ABSTRACT

HUANG, CHING-WEI. Effect of Microscale Turbulent Structures Dynamics on Forced Convection in Turbulent Porous Media Flow. (Under the direction of Dr. Andrey V. Kuznetsov).

Turbulent porous media flow commonly occur in various applications such as canopy flows, pebble bed nuclear reactors, heat exchangers, porous chemical reactors, and crude oil extraction. Studies for porous media flow have been more emphasized on the macroscale level. The influence of microscale flow structures (smaller than the pore size) on turbulent heat transfer in porous media has not yet been investigated systematically. The goal of this study is to investigate the turbulence flow structures in porous media and the influence they have on convection heat transfer in porous media flow. Investigation was done by simulations using a Representative Elementary Volume (REV) with 4×4 cylindrical obstacles. Periodic boundary conditions were used to represent the infinite porous medium structure.

To find out the scales of turbulent flow structures in porous media flow, we investigated the relation between the pore size versus turbulence intensity (I_t) and turbulence length scale (l_t). This was to address a paradox between turbulence generation by a single solid obstacle and turbulence suppression by multiple solid obstacles. In a clear fluid region, a single obstacle will act as a turbulence enhancer, with the enhancement being proportional to the obstacle size. Unlike around a single obstacle, turbulence in a porous medium is restricted by the surfaces of other obstacles surrounding it. This restriction is expected to be proportional to the distance between the surfaces of the two neighboring obstacles.

The microscale flow structures (smaller than the pore size) in porous media flow influence the heat transfer from the solid obstacles comprising the porous medium to the fluid. Turbulent flow in a homogeneous porous medium was investigated using Large Eddy Simulation

(LES). We observed that the convection heat transfer characteristics are dependent on whether the micro-vortices are attached or detached from the surface of the obstacle. There is a spectral correlation between the Nusselt number and the pressure instabilities due to vortex shedding. A secondary flow instability occurs due to high pressure regions forming periodically near the converging pathway between obstacles. This causes local adverse pressure gradient, affecting the flow velocity and convection heat transfer. This study has been performed for obstacles with shapes of square and circular cylinders at porosities of 0.50 and 0.87. Understanding the dominant modes that affect convection heat transfer can aid in finding an optimum geometry for the porous medium.

Effect of Microscale Turbulent Structures Dynamics on Forced Convection in Turbulent Porous Media Flow

by
Ching-Wei Huang

A dissertation submitted to the Graduate Faculty of
North Carolina State University
in partial fulfillment of the
requirements for the degree of
Doctor of Philosophy

Aerospace Engineering

Raleigh, North Carolina
2021

APPROVED BY:

Dr. Andrey V. Kuznetsov Committee Chair	Dr. Alexei V. Saveliev
Dr. Tarek Echekki	Dr. Pramod Subbareddy

DEDICATION

This dissertation is dedicated to my parents and grandparents for their care and support. To Vishal who helped me with everything in this dissertation. To Anndy, the supplier of cat pictures and late-night study buddy.

BIOGRAPHY

The author was born in Tainan, Taiwan, a city known for its foods and culture. He earned his bachelor's degree in Computer Science from National Chengchi University (NCCU) in Taipei, Taiwan. After that, he pursued his masters in Power Mechanical Engineering from National Tsing Hua University (NTHU) in Hsinchu, Taiwan. Finally, he joined North Carolina State University (NCSU) to continue his doctoral research in the field of Aerospace Engineering. He worked under the guidance of Dr. Andrey V. Kuznetsov in the domain of the turbulence in porous media flow. Outside academics, Ching-Wei enjoys volleyball, sketching and travelling.

TABLE OF CONTENTS

LIST OF TABLES

LIST OF FIGURES

CHAPTER 1

Introduction

1.1 Background

Flows in a porous media is an important area of study due to the wide range of its applications, including heat exchanger design, filter efficiency prediction, and biomechanics of kidney and liver [1]. One of the important topics for flows in porous media is whether macroscopic turbulence, characterized by turbulent structures larger than the pore size, can exist in a porous medium [2].

The modeling of turbulence in porous media, based on both pore-scale turbulence and large-scale turbulence, has been reviewed by de Lemos [3] and more recently by Nield and Bejan [1]. Models that relied on a large-scale (macroscale) turbulence approach were developed by Lee and Howell [4], Prescott and Incropera [5], Antohe and Lage [6] as well as by other researchers. Nield [7,8] suggested that the pore scale could limit the size of turbulent eddies. Recent studies by Jin et al. [2], Uth et al. [9], and Jin and Kuznetsov [10] used Direct Numerical Simulation (DNS) of forced convection flows in porous media which suggested that the pore size of the porous medium determines the maximum size of turbulent eddies. Due to the restriction on the size of turbulent eddies, turbulent kinetic energy is unable to transfer from larger to smaller turbulent eddies. This in turn prevents large scale turbulence. This suggests that turbulence in a porous medium, due to its much smaller intensity, acts differently from turbulence in a clear fluid. For the case of a bidispersed porous medium, characterized by two significantly different pore scales, there may even be a second critical Reynolds number. It is possible that, when

involving flows in composite porous/fluid domains, a flow in a porous region may be approximated as laminar even though a flow in a clear fluid region is turbulent [11,12].

Porous media are commonly used in heat exchangers to enhance thermal efficiency due to their high surface contact area per unit volume, which helps to enhance the heat transfer rate. Microscopic vortices, caused by flow interaction with solid obstacles, have a significant influence on heat transfer. We examine the characteristics of microscopic vortices and their influence on heat transfer in turbulent porous media flow. Convection in porous media has been reviewed by Nield and Bejan [1], discussing factors such as pressure changes, viscous dissipation, and lack of local thermal equilibrium. Nakamura et al. [13] reported that for flow over a single cylinder, the relation between the Nusselt number and Reynolds number varies greatly for different flow regimes, which correspond to different lengths of the vortex formation region behind the cylinder. Similar correlations of the Nusselt number and Reynolds number were reported in studies of convection heat transfer for an array of obstacles. Direct numerical simulations were conducted for uniformly spaced squares, circular rods, and spheres by Kuwahara et al. [14]. McCarthy [15] performed Lattice gas cellular automata simulations for flow through arrays of cylinders. Although extensive work has been done for the macroscopic heat transfer in convection flow in porous media, the various effects of the microscopic vortices on heat transfer in different conditions have yet to be explored thoroughly.

There has not yet been a systematic study on the influence of microscale flow structures (smaller than the pore size) on turbulent heat transfer in porous media [16]. Models of turbulent porous media flow are useful for the systematic study for applications such as canopy flows, pebble bed nuclear reactors, heat exchangers, porous chemical reactors, and crude oil extraction [17]. Macroscopic turbulence models for porous media flows have been developed throughout

the years [18–21], combining the Volume Average Theory (VAT) [22] with Reynolds Averaging (RA). Reynolds Averaged Navier-Stokes (RANS) simulations of microscale porous media flow have been used to determine coefficients for the RA-VAT models [23–25]. However, the results from microscale RANS simulations are constrained by the modelling error [26].

Jin et al. [27] and Uth et al. [28] performed Direct Numerical Simulation (DNS) of forced convection flows in porous media, which suggested that the pore size of the porous medium determines the maximum size of turbulent eddies. The study led to the development of a mixing-length macroscale model based on the mixing layer hypothesis by Jin & Kuznetsov [29]. DNS studies by He et al. [30] verified that the turbulence integral length scale is ~10% of the obstacle diameter in a closely packed porous medium. Turbulent energy transport is crucial for studying convection heat transfer in porous media. Several macroscopic energy models have been developed that make use of the gradient diffusion hypothesis in conjunction with the assumption of thermal equilibrium between the solid and fluid phases [25], [31].

Microscale studies show that the heat transfer efficiency between the obstacle surface and the fluid increases with an increase in the Reynolds number and obstacle diameter [32,33]. The microscale simulations for square rods [31], circular rods [34], and elliptic rods [35] revealed that the thermal dispersion varies drastically with the obstacle shape. The functional dependence of the Nusselt number on porosity changes with the obstacle shape [36]. High Resolution LES studies of finite pebble beds show that hot spots appear on the surface of the pebbles are highly unsteady, in which their locations move over time [37], highlighting the importance of a transient analysis. The microscale distribution of the Nusselt number from DNS studies [32] shows that the unsteady wake region contributes the least towards heat transfer. Turbulent thermal mixing

for circular rods increases with an increase in the Reynolds number and approaches an asymptotic value at higher Reynolds numbers [38].

The influence of microscale flow structures (smaller than the pore size) on turbulent heat transfer in porous media has not yet been investigated systematically. The goal of this study is to investigate the turbulence flow structures in porous media and the influence they have on convection heat transfer in porous media flow.

1.2 Thesis Objectives

In this thesis, we study the microscopic flow physics that impact heat convection in turbulent porous media flow. Simulations were done by using RANS and LES methods to simulate the microscopic flow field.

In chapter 2, we investigated the relation between the pore size and turbulence intensity for flows in porous media. Our goal is to address a paradox between turbulence generation by a single solid obstacle and turbulence suppression by multiple solid obstacles. We verify that the turbulence length scale is restricted by the surfaces of the surrounding obstacles. The turbulence length scale thus should be comparable to the pore size.

In chapter 3, we investigate the relation concerning the rate of heat transfer between the obstacle surface and the fluid (q_{avg}). The size of the contact area between the vortices and the solid obstacles in the porous medium (A_{vc}) is shown to have a considerable effect on the overall heat transfer from the obstacle to the fluid under the same Reynolds number. Factors such as the porosity (φ), Pore Scale Reynolds number (Re_p), and obstacle shape of the porous medium were investigated. All three of these factors have different influences on the contact area A_{vc}, and, by extension, the overall heat transfer rate q_{avg}.

In chapter 4, we investigate the influence of the micro-vortices on convection heat transfer in turbulent porous media flow. The convection heat transfer characteristics are dependent on whether the micro-vortices are attached or detached from the surface of the obstacle. The correlation between the Nusselt number and the pressure instabilities due to vortex shedding is looked at. A secondary flow instability occurs due to high pressure regions forming periodically near the converging pathway between obstacles.

1.3 Representative Elementary Volume

A Representative Elementary Volume (REV) was used in order to simulate an infinite periodic matrix. The REV is defined as the smallest sub-volume that shows the same behavior as the flow in the whole porous domain. Uth et al. [9] performed a DNS study of turbulent forced convection in porous media and reported that the largest scale of turbulence structures observed in their study was approximately four times the distance between centers of the obstacles, *s*. Thus, a REV with a side length of 4*s* is assumed to be a sufficiently large size to capture the largest turbulent eddies in the porous medium. Cylindrical solid obstacles have been arranged in a simple square lattice to represent a homogeneous, anisotropic porous medium. A three-dimensional simulation domain (see **Figure 1.1**) has been constructed using 4 unit cells along the *x*- and *y*- directions, and 2 unit cells in the *z*- direction based on the inferences from Jin et al. [27] and Uth et al. [28], forming a $4s \times 4s \times 2s$ Representative Elementary Volume (REV).

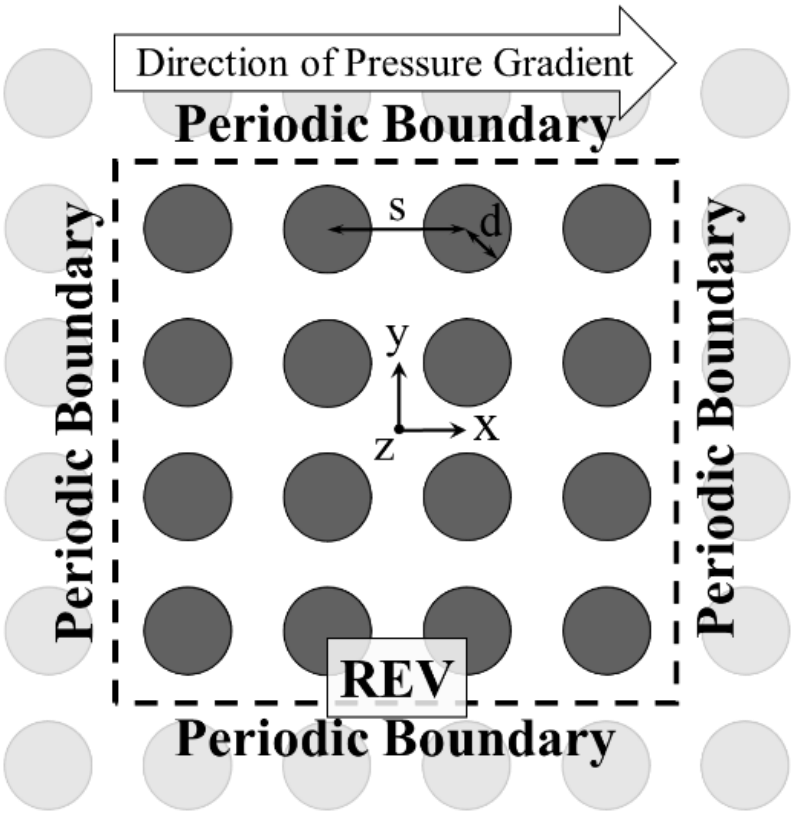

Figure 1.1 The REV, marked by the dashed lines, for a homogeneous porous medium with infinite cylindrical obstacles. The distance between centers of the obstacles *s* and the obstacle diameter *d* are also shown in the figure.

In our computations, the porosity φ and the Pore Scale Reynolds number Re_p are defined as follows.

$$\varphi = 1 - \frac{\pi}{4}\left(\frac{d}{s}\right)^2 \tag{1.1}$$

$$Re_p = \varphi \cdot \frac{u_{m,x} d}{\nu} \tag{1.2}$$

where d is the diameter of cylindrical obstacles, $u_{m,x}$ is the mean velocity in the x-direction, and ν is the kinematic viscosity of the fluid.

CHAPTER 2

Effects of the Pore Size on Turbulence Intensity and Turbulence Length Scale

2.1 Abstract

In this chapter, we investigate the relation between the pore size and turbulence intensity for flows in porous media. Our goal is to address a paradox between turbulence generation by a single solid obstacle and turbulence suppression by multiple solid obstacles. In a clear fluid region, a single obstacle will act as a turbulence enhancer, with the enhancement being proportional to the obstacle size. Unlike around a single obstacle, turbulence in a porous medium is restricted by the surfaces of other obstacles surrounding it. This restriction is expected to be proportional to the distance between the surfaces of the two neighboring obstacles.

To further understand the effects of porous media on turbulent flows and to better understand the relation between the pore scale and turbulence intensity, we compared flows in porous media with different pore sizes. We discuss the change in the distribution of turbulence intensity as well as changes in the flow field pressure and velocity distributions caused by the change in the pore size. The Reynolds number that describes the pore-scale turbulence should be dependent on a certain characteristic length of the porous medium geometry. This length is likely to be the hydraulic diameter of the pore cross section if we treat the flow as an internal flow, or the distance between the obstacles' surfaces if we view it as an external flow.

A representative elementary volume (REV) with 4×4 cylindrical obstacles to represent the infinite porous medium structure was used (**Figure 1.1**). The REV has periodic boundaries in the *x*, *y* and *z*-directions, and a specified mass flow rate in the *x*-direction. Changing the cylinder diameter, *d*, under a constant Reynolds number of approximately 5,000, we compared the

macroscopic turbulence intensity, $I_{t,macro}$, the location of maximum turbulence intensity, $I_{t,max}$, and the maximum turbulence length scale, $l_{t,max}$, for each case. Although the driving force (the applied pressure gradient) acts only in the *x*-direction, we observed a mean velocity in the *y*-direction, and a noticeable change in the bulk flow direction for the $d/s = 0.8$ case, where *s* is the distance between centers of the obstacles. We found that $I_{t,macro}$ increases in the range $d/s = 0.1{\sim}0.4$ with increased *d*, then slightly decreases in the range $d/s = 0.6{\sim}0.8$. We think this is caused by the turbulence suppression from cylinder walls. We also observed the bulk flow direction deviating from the direction of the applied pressure gradient, which could also contribute to the slight decrease of $I_{t,macro}$ in these cases. The location of $I_{t,max}$ changes from near the separation point slightly behind each cylinder for $d/s = 0.1{\sim}0.2$, to the location where the wake comes into contact in the front of each cylinder for $d/s = 0.4{\sim}0.8$. This suggests that the turbulence generated by a cylinder is being suppressed by the surrounding cylinders. The maximum turbulence length scale decreases with increased d throughout the range of $d/s = 0.1{\sim}0.8$. There is a large decrease in the range $d/s = 0.1{\sim}0.2$, which we believe is the result of turbulence structures generated from each cylinder starting to interact with the surrounding cylinders.

Although further confirmation of these results is required, this study provides an estimate on how the pore size may affect the turbulent flow in porous media with large solid obstacles.

2.2 Methods

2.2.1 Geometry

In order to simulate an infinite periodic matrix, we used a representative elementary volume (REV). The size of the REV is $4s \times 4s \times 2s$ in the x, y, and z-directions respectively, as shown in **Figure 1.1**. The REV consists of 4×4 cylindrical obstacles whose center points are a distance s apart in the x and y-directions. In our computations, the diameter of the cylinder d is varied from $0.1s$ to $0.8s$. The porosity φ and pore scale Reynolds number Re_p for this geometry is calculated as equations (1.1) and (1.2).

2.2.2 Boundary Conditions

Periodic boundary conditions were used in the x, y and z-directions, respectively, with a specified mass flow rate, $\dot{m}$, in the x-direction to keep the Reynolds number constant. No-slip boundary conditions were used on the walls of the cylindrical obstacles.

2.2.3 Models

The Reynolds Averaged Navier-Stokes (RANS) model used in this study is the realizable k-ε model. Computations were performed using the commercial software ANSYS FLUENT 18.1 (ANSYS, Canonsburg, Pennsylvania) [39].

The Reynolds Averaged Navier-Stokes equations with the linear eddy-viscosity approximation of the Reynolds Stresses are written in equations (2.1)-(2.2) (the overbar notation denotes time averaging). The Realizable k-ε model approximates the turbulence eddy viscosity (μ_T) by solving equations (2.3)-(2.4) for the turbulence kinetic energy (k) and the turbulence

dissipation rate (ε). The turbulence eddy viscosity is calculated using equation (2.5). The model is closed according to the constants and relations provided in the work of Shih et al. [40].

$$\frac{\partial}{\partial x_i}(\rho \bar{u}_i) = 0 \tag{2.1}$$

$$\frac{\partial}{\partial x_j}\left(\rho \bar{u}_i \bar{u}_j\right) = -\frac{\partial \bar{p}}{\partial x_i} + \frac{\partial}{\partial x_j}\left[(\mu + \mu_T)\left(\frac{\partial \bar{u}_i}{\partial x_j} + \frac{\partial \bar{u}_j}{\partial x_i}\right)\right] + \rho g_i \tag{2.2}$$

$$\frac{\partial(\rho k \bar{u}_j)}{\partial x_j} = \frac{\partial}{\partial x_j}\left[\left(\mu + \frac{\mu_T}{\sigma_k}\right)\frac{\partial k}{\partial x_j}\right] + 2\mu_T \bar{S}_{ij}\bar{S}_{ij} - \rho\varepsilon \tag{2.3}$$

$$\frac{\partial(\rho \varepsilon \bar{u}_j)}{\partial x_j} = \frac{\partial}{\partial x_j}\left[\left(\mu + \frac{\mu_T}{\sigma_\varepsilon}\right)\frac{\partial \varepsilon}{\partial x_j}\right] + \rho C_1 \sqrt{2\bar{S}_{ij}\bar{S}_{ij}}\,\varepsilon - \rho C_2 \frac{\varepsilon^2}{k + \sqrt{\mu\varepsilon/\rho}} \tag{2.4}$$

$$\mu_T = \rho C_\mu \frac{k^2}{\varepsilon};\ \bar{S}_{ij} = \frac{1}{2}\left(\frac{\partial \bar{u}_j}{\partial x_i} + \frac{\partial \bar{u}_i}{\partial x_j}\right) \tag{2.5}$$

In the vicinity of the wall, the transport equation for turbulence dissipation rate is not solved. The value of ε is estimated using equations (2.6)-(2.7). The one-equation model is invoked whenever the wall-distance-based Reynolds number (defined as Re_y in equation (2.8); y is the distance to the nearest wall) drops below a threshold value of 200, signifying the dominance of molecular viscosity. A blending function is used to bridge the interface between the one- and two- equation models. The turbulence eddy viscosity is calculated using equation (2.8) for the one-equation model. The model constants are available in the ANSYS documentation [39].

$$\varepsilon = \frac{k^{1.5}}{l_\varepsilon} \tag{2.6}$$

$$l_\varepsilon = yC_l^*\left(1 - e^{\frac{-Re_y}{A_e}}\right);\ l_\mu = yC_l^*\left(1 - e^{\frac{-Re_y}{A_\mu}}\right) \tag{2.7}$$

$$\mu_{T_{2-Layer}} = \rho C_\mu l_\mu \sqrt{k};\ Re_y = \frac{y\sqrt{k}}{\nu} \tag{2.8}$$

The Finite Volume Method (FVM) is used to solve the governing equations. The derivatives are approximated using a second-order upwind scheme for the convective terms and a second-order central scheme for the viscous terms. The location of the pressure variable is staggered such that it is stored at the centroid of the face of the cell. The governing equations are solved in a segregated manner using the SIMPLE algorithm. The momentum source term g_i is adjusted at every iteration to maintain a constant flow rate at the periodic boundaries. Since the flow is incompressible, this translates to an indirect specification of the Reynolds number through the macroscopic velocity (see equation (1.2) for the definition of the Pore Scale Reynolds number). The fluid material is chosen to be water since the solver uses the dimensional form of the governing equations. The results are non-dimensionalized before processing.

The velocity u was represented as a combination of the mean velocity, $\bar{u}$, and the unsteady fluctuation velocity, u':

$$u = \bar{u} + u' \tag{2.9}$$

where $\bar{u}$ was calculated from the three mean velocity components in the *x*, *y*, and *z*-directions and $u'$was calculated by the root-mean-square of the turbulent velocity fluctuations. To investigate the effect of the obstacle size on turbulence, we compared the turbulence

intensity, I_t, the macroscopic turbulence intensity, $I_{t,macro}$, and the turbulence length scale, l_t, defined as:

$$I_t = \frac{u'}{\bar{u}} \tag{2.10}$$

where k is the turbulence kinetic energy and ε is the turbulence dissipation rate calculated from the realizable k-ε model. $\langle k \rangle$ and $\langle U \rangle$ are the volume averaged values of turbulence kinetic energy and velocity magnitude, respectively.

2.2.4 Validation and Accuracy

To validate our simulation results, we compared our computational data for the drag coefficient C_d for a flow over a single cylinder, obtained using the same meshing, geometric and boundary conditions as for the REV, with experimental data for a flow over a single cylinder [41]. This allowed us to verify that the model is capable to accurately predict the boundary layer flow around the cylinder, as well as the drag force between the surface of the cylinder and the flow.

A large eddy simulation (LES) was preformed to verify and further examine the results for the $d/s = 0.8$ case.

2.3 Results and Discussion

2.3.1 Velocity Distribution

To minimize errors caused by the boundary conditions, we presented data on the plane $z = 0.5s$. We maintained a constant Reynolds number of 5,000 by specifying an *x*-direction mass flow rate in the boundary conditions. This Reynolds number determines the mean *x*-direction velocity of the flow field, U_x. The corresponding porosity for each case is shown in **Table 2.1**.

In the $d/s = 0.2{\sim}0.4$ cases, as shown in **Figure 2.1** (a) (b), the flow around the rows of cylinders in the *x*-direction barely interacts with the flow around neighboring rows. This forms a "duct"-like region between the two rows of cylinders in the *x*-direction. The vortices in the wake behind a cylinder are attached to the cylinder's wall. The vortex core size is not restricted by the next cylinder in the *x*-direction, and the flow field is generally symmetric.

For larger cylinders ($d/s = 0.6{\sim}0.8$), the vortices behind the cylinders propagate at an angle to the principal flow direction, forming a mean velocity in the *y*-direction. The mean *y*-velocity can be directed upward or downward; these two cases are analogous. Consider the situation where the mean *y*-velocity is directed upward. This aids in the identification of the top and bottom half of the cylinder. Our LES results for the $d = 0.8s$ case suggest that the change in the bulk flow's direction is caused by the pressure gradient from the diverging and converging walls of the cylinders. This pressure gradient forces the shedding vortices that are first formed in the developing stage of the flow to recirculate and break down into smaller vortices. After the von Karman instability is formed, it creates an uneven shedding of the vortices behind these cylinders. These uneven vortices interact with the recirculating vortices that have broken down

and form uneven vortices on the top and bottom side behind the cylinder. This creates a pressure difference between the uneven vortices, driving the flow in the *y*-direction.

In the $d/s = 0.8$ case, as shown in **Figure 2.1** (d), we observed the bulk flow deviating from the principal flow direction significantly (~30^o). Iacovides et al. [42] reported a similar deflection of the flow over in-line tube banks. In this case the distance between the bottom separation point and the stagnation point on the horizontally adjacent cylinder is smaller, causing the bottom side separation point to be shifted downstream by the high pressure region near the stagnation point. This keeps the bottom side separation point near the throat formed by two horizontally aligned cylinders, resulting in a significant increase of the mean velocity in the *y*-direction. The mean *y*-velocity for various d/s ratios is reported in Table 1. The LES result for the $d/s = 0.8$ case is shown in

Figure 2.2, where we can see the formation of the flow field. This phenomenon is explored in our recent work [43].

Table 2.1 Computational results for the mean velocity and porosity.

$\boldsymbol{d/s}$	0.1	0.2	0.4	0.6	0.8
$\boldsymbol{\varphi}$	0.992	0.968	0.874	0.717	0.497
$\boldsymbol{U_y/U_x}$	3.27E-05	2.90E-05	4.29E-04	2.50E-01	6.78E-01

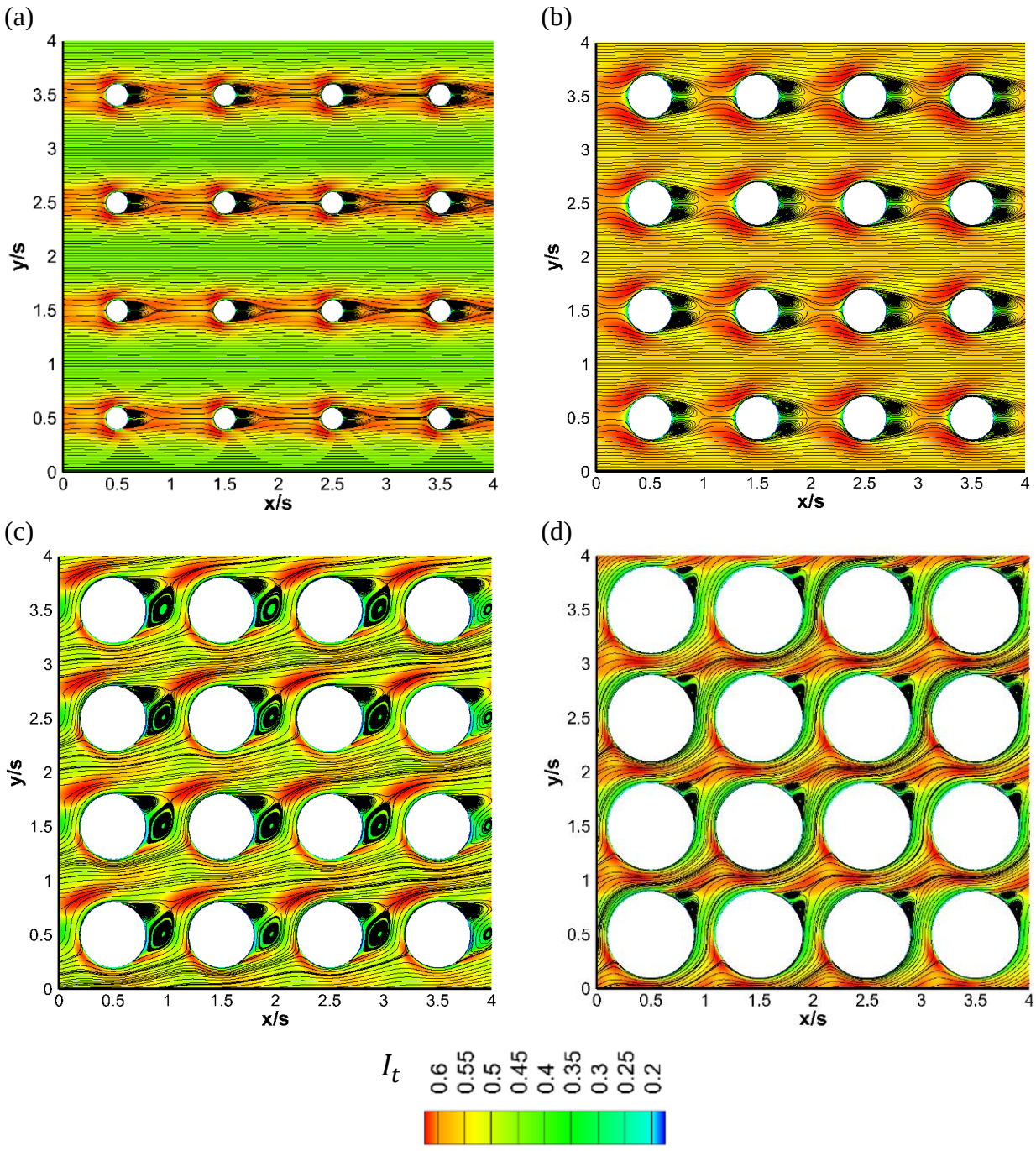

Figure 2.1 Streamlines and turbulence intensity distributions in the REV. (a) $d/s = 0.2$; (b)$d/s = 0.4$; (c)$d/s = 0.6$; (d)$d/s = 0.8$.

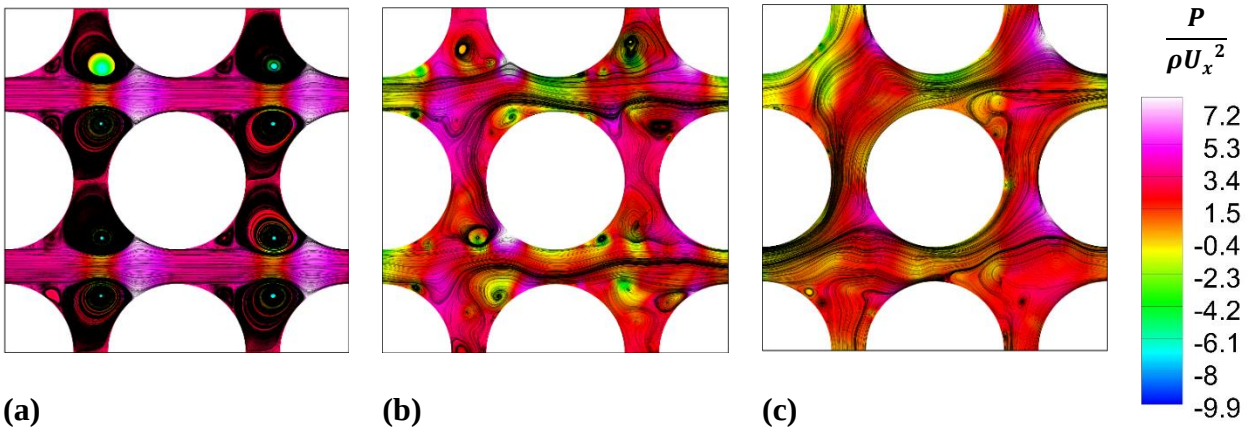

Figure 2.2 Streamlines and pressure contour obtained from LES results of$d/s = 0.8$ case, showing the formation of the change in the bulk flow direction. (a) High pressure gradient from converging walls between two cylinders forces the shedding vortices to recirculate; (b) Uneven vortices form a pressure gradient, which drives the flow in the *y*-direction; (c) Delayed bottom separation point and change in the bulk flow direction.

2.3.2 Turbulence Intensity

The simulation results show that for $d/s = 0.1{\sim}0.4$, the macroscopic turbulence intensity, $I_{t,macro}$, increases with increased d, and then slightly decreases in the range $d/s = 0.4{\sim}0.8$, as shown in **Figure 2.3** (a). This agrees with our assumption that the obstacles promote turbulence, but the walls of surrounding obstacles act as a restriction of turbulence in the flow. The bulk flow deviating from the driving force direction could also contribute to the slight decrease in $I_{t,macro}$ for $d/s = 0.6{\sim}0.8$.

By comparing the contours of the turbulence intensity I_t for different cases in **Figure 2.1**

Streamlines and turbulence intensity distributions in the REV. (a)$d/s = 0.2$; (b)$d/s = 0.4$; (c)$d/s = 0.6$; (d)$d/s = 0.8$., we can see that the location of the maximum turbulence intensity, $I_{t,max}$, changes for different porosities. For $d/s = 0.1{\sim}0.2$, the location of $I_{t,max}$ is near the separation points behind each cylinder, as shown in **Figure 2.1** (a). For ($d)/s = 0.4$,

the location of $I_{t,max}$ changes to where the wake impinges on the front of the cylinder, and the magnitude of turbulence intensity near the separation point becomes relatively low, as shown in **Figure 2.1**(b). This shows that the cylinder wall downstream is suppressing the turbulence of the shedding vortices from the cylinder upstream. As the mean velocity in the *y*-direction starts to appear at $d/s = 0.6$, the location of $I_{t,max}$ shifts downstream of the shedding vortices' path, as shown in **Figure 2.1** (c). Due to deviation in the flow direction, the shedding vortices can dissipate in the flow, which decreases turbulence suppression by the downstream cylinder. This can be seen from the magnitude of I_t near the lower separation point increasing and becoming comparable to $I_{t,max}$. After a significant change in the mean flow direction, in the $d/s = 0.8$ case (**Figure 2.1** (d)), the shedding vortices again impinge on the front of the cylinder downstream, suppressing the turbulence of the wake, and decreasing the magnitude of I_t near the lower separation point. These changes in the I_t distribution for different porosities suggest that the obstacle simultaneously generates turbulence and suppresses turbulence generated by the other obstacles.

2.3.3 Turbulence Length Scale

Comparing the maximum turbulence length scale, $l_{t,max}$, for each case, we can see that $l_{t,max}$ first decreases with increasing d in the range $d/s = 0.1\sim0.2$ and then remains approximately constant in the range $d/s = 0.2\sim0.4$ (**Figure 2.3** (b)). It then decreases with the increasing obstacle diameter until $d/s = 0.8$. These results agree with our hypothesis that $l_{t,max}$ is restricted by the surfaces of the neighboring obstacles. We think the first drop in $l_{t,max}$ in the range $d/s = 0.1\sim0.2$ is caused by the downstream cylinder starting to interact with the wake

from the upstream cylinder in a horizontal row. Then in the range $d/s = 0.2\sim0.4$, the vortices that are dissipated on the downstream cylinder wall start to affect the "duct" flow region between two rows of cylinders. The effect slightly increases the turbulent kinetic energy and balances out the increased restriction from the walls, resulting in $l_{t,max}$ staying relatively constant. In the range $d/s = 0.6\sim0.8$, because of the change in bulk flow direction, the vortices behind a cylinder dissipate in the bulk flow instead of on the downstream cylinder wall. The vortices also become smaller as d grows larger, generating less turbulent kinetic energy. We can also see that $l_{t,max}$ continues to be restricted by the surfaces of neighboring obstacles.

We conclude that a value of d/s at which the turbulence length scale takes on its maximum value $l_{t,max}$ occurs before the obstacle walls start to restrict the size of turbulence structures, which happens before $d/s = 0.2$.

(a)

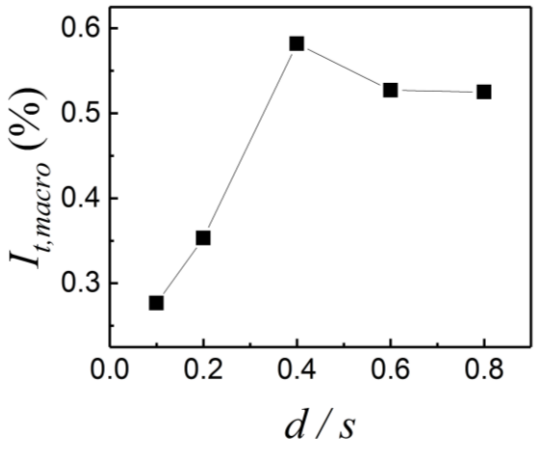

(b)

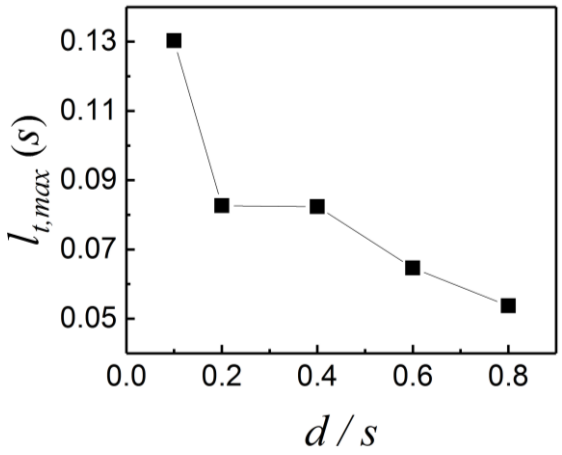

(c)

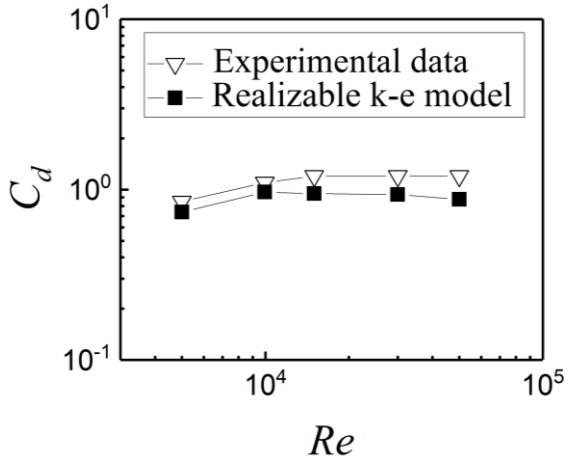

Figure 2.3 (a) Turbulence intensity variation with the change in the diameter of the cylindrical obstacle, characterized by d/s; (b) Turbulence length scale variation with the change in the cylindrical obstacle diameter, characterized by d/s; (c) Comparison of the drag coefficients for flow over a single cylinder obtained computationally by using a realizable *k*-*ε* model and the experimental data of Panton et al. [41].

2.3.4 Drag Coefficient Comparison

By controlling the mass flow rate, we used five different Reynolds numbers for the comparison: 5,000; 9,950; 15,000; 30,000; and 50,000. From these results, we can see that when

the Reynolds number increases, the drag coefficient becomes almost constant. This is similar to the behavior of the experimental data, as shown in **Figure 2.3** (c).

The results show that our simulation slightly underpredicts the drag acting on the cylindrical surface. This deviation may be caused by insufficient mesh resolution or by the utilization of a realizable *k*-ε model. We will modify the meshing and compare the simulation results of other models to improve the accuracy in future studies.

2.4 Conclusions

We used the realizable *k*-ε model to simulate a turbulent flow in a porous medium. By analyzing the turbulence intensity and turbulence length scale, we can see that the results support our hypothesis, first expressed in Jin et al. [2], which states that the turbulence length scale is restricted by the surfaces of the surrounding obstacles. The turbulence length scale thus should be comparable to the pore size. We also observed an interesting phenomenon in low porosity cases of $\varphi \leq 0.717$ ($d/s = 0.6{\sim}0.8$), where the bulk flow direction deviates from the driving force direction, and the flow becomes non-symmetric, even though the boundary conditions and geometry are symmetric. Although further confirmation of these findings is required, this study provides an estimate of how the pore size may affect turbulent flow in a porous medium.

The physics and parameters that control the observed change in the bulk flow direction at low porosities will be studied further in future research. Simulations of flows in porous media with a constant mass flow rate and different obstacle shapes will also be of interest for future studies. More DNS and LES studies are required to further confirm the obtained results.

CHAPTER 3

Surface Contact Area Between Microscopic Vortices and Solid Obstacle Surfaces

3.1 Abstract

Porous media are commonly used in heat exchangers to enhance thermal efficiency due to their high surface contact area per unit volume, which helps to enhance the heat transfer rate. Microscopic vortices, caused by flow interaction with solid obstacles, have a significant influence on heat transfer. Convection in porous media has been reviewed by Nield and Bejan [1], discussing factors such as pressure changes, viscous dissipation, and lack of local thermal equilibrium.

In the previous chapter, we established that the turbulence length scale is restricted by the surfaces of the surrounding obstacles. The turbulence length scale thus should be comparable to the pore size of the porous medium geometry. When changing the porosity, we observe a large variation in the microscale turbulence properties (Turbulence intensity and turbulence length scale). Therefore we expect the influence of the microscale turbulence on heat convection to be substantial.

Although extensive work has been done for the macroscopic (smaller than the pore size) heat transfer in convection flow in porous media, the various effects of the microscopic vortices on heat transfer in different conditions have yet to be explored thoroughly.

In this chapter, we examine the characteristics of microscopic vortices and their influence on heat transfer in turbulent porous media flow. Turbulent flow in a homogeneous porous medium was investigated through the use of numerical methods by employing the Reynolds Averaged Navier-Stokes (RANS) modeling technique. The focus of our research was to study

how microscopic vortices in porous media flow influence the heat transfer from the solid obstacles comprising the porous medium to the fluid. A Representative Elementary Volume (REV) with 4×4 cylindrical obstacles and periodic boundary conditions was used to represent the infinite porous medium structure (**Figure 1.1**).

Our hypothesis is that the rate of heat transfer between the obstacle surface and the fluid (q_{avg}) is strongly influenced by the size of the contact area between the vortices and the solid obstacles in the porous medium (A_{vc}). This is because vortices are regions with low velocity that form an insulating layer on the surface of the obstacles. Factors such as the porosity (φ), Pore Scale Reynolds number (Re_p) (defined in equations (1.1) and (1.2)), and obstacle shape of the porous medium were investigated. All three of these factors have different influences on the contact area A_{vc}, and, by extension, the overall heat transfer rate q_{avg}. Under the same Pore Scale Reynolds number (Re_p), our results suggest that a higher overall heat transfer rate is exhibited for smaller contact areas between the vortices and the obstacle surface. Although the size of the contact area, A_{vc}, is affected by Re_p, the direct influence of Re_p on the overall heat transfer rate q_{avg} is much stronger and exceeds the effect of A_{vc} on q_{avg}. The Pore Scale Reynolds number, Re_p, and the mean Nusselt number, Nu_m, have a seemingly logarithmic relationship.

3.2 Methods

A Representative Elementary Volume (REV) was used in order to simulate an infinite periodic matrix. The REV is $4s$×$4s$×$2s$ in the *x*, *y*, and *z*-directions respectively, as shown in

Figure 1.1. The REV consists of 4×4 cylindrical obstacles whose center points are a distance *s* apart in the *x* and *y*-directions.

Periodic boundary conditions were used in the *x*, *y*, and *z*-directions, respectively. A mass flow rate, $\dot{m}$, was specified in the *x*-direction to match the desired Pore Scale Reynolds number (Re_p) (defined in equation (1.2)). The porosity of the REV is defined in equation (1.1). No-slip boundary conditions were used on the walls of cylindrical obstacles. The temperature of the walls of the cylindrical obstacles was set to a constant value of 353K, while the average temperature of the inlet flow was set to 323K. With this boundary condition setting, the characteristic temperature difference, ΔT, was 30K.

The turbulence model used in this study was the realizable *k*-*ε* model. Computations were performed using the commercial software ANSYS FLUENT 18.1 (ANSYS, Canonsburg, Pennsylvania) [39].

For validation of our results, a Large Eddy Simulation (LES) study for a REV consisting of cylindrical obstacles was performed to verify results with the *k*-*ε* model at $\varphi = 0.497$ and $Re_p = 500$. A comparison of the RANS and LES results is discussed in the Reynolds Number section in Results and Discussion. A grid independence study was performed for the case of $\varphi = 0.497$ at $Re_p = 5000$ for cylindrical obstacles representing the porous medium. The y^+ values were kept at 1 near the walls while the maximum grid size was altered. RANS results were compared while decreasing the grid size until the changes of the applied pressure gradient and the average Nusselt number Nu_m were below 1%. Nu_m is defined as

$$Nu_m = \frac{\bar{h}d}{k} = \frac{q_{avg}}{k(\Delta T)/d} \tag{3.1}$$

3.3 Results And Discussion

3.3.1 Porosity

We investigated the influence of porosity on the microscopic vortices and, by extension, the effects of porosity on heat transfer between the obstacle surface and fluid (q_{avg}). The Pore Scale Reynolds number was kept constant at $Re_p = 5000$ and the porosity was varied by adjusting the distance between neighboring obstacles *s*.

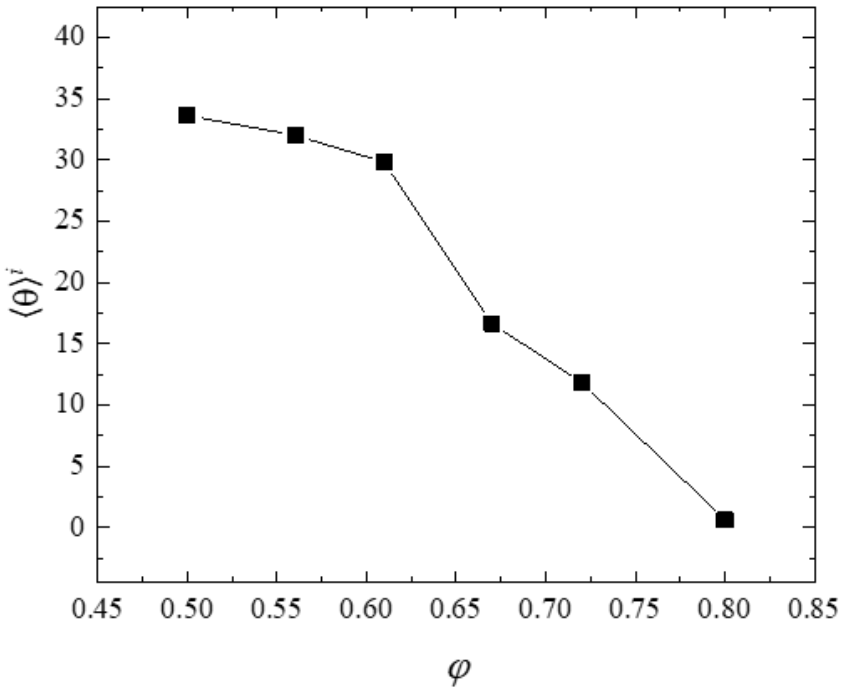

Figure 3.1 Variation of macroscopic flow angle $\langle\theta\rangle^i$ with porosity for circular cylindrical obstacles.

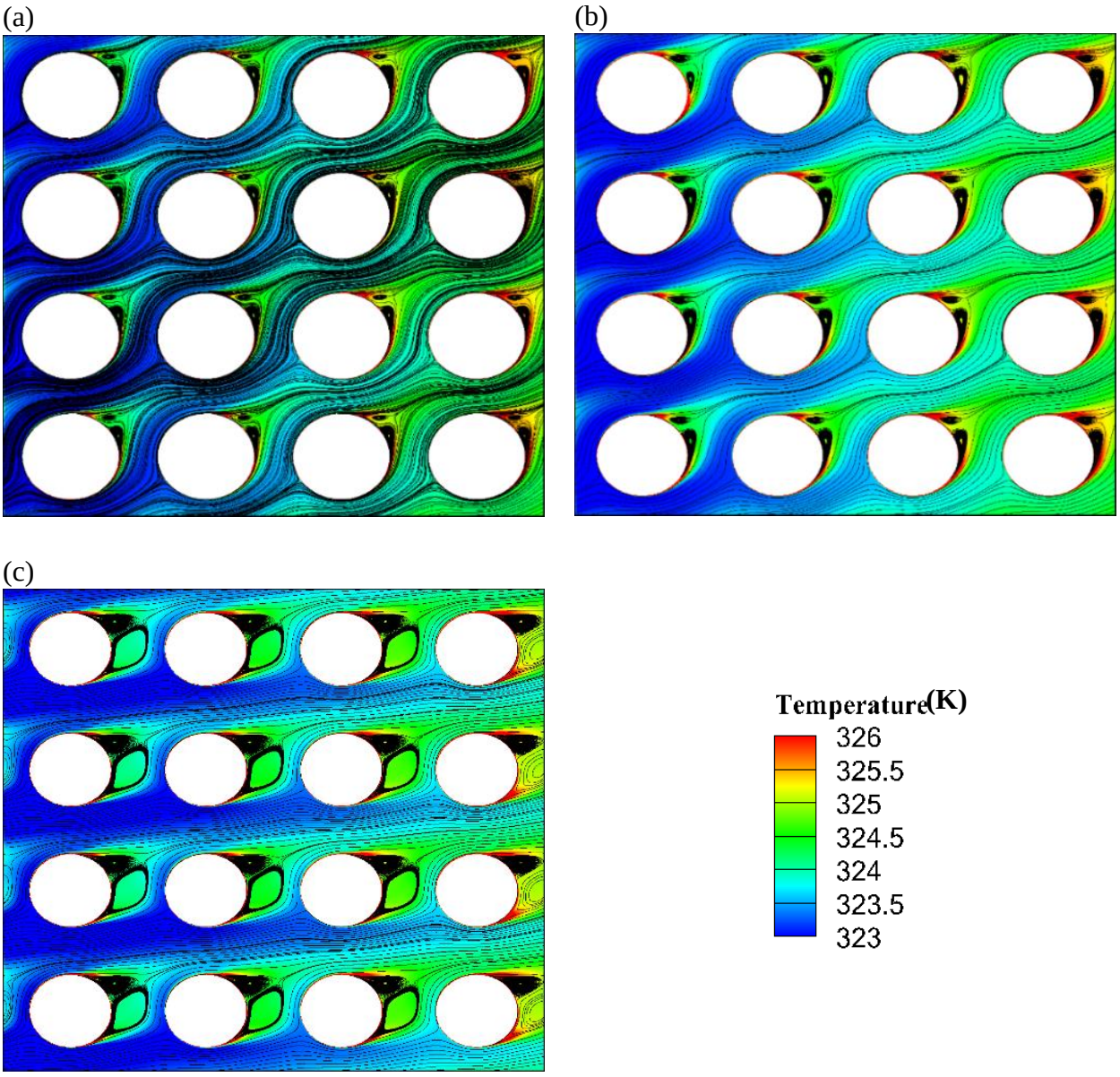

Figure 3.2 Streamlines and temperature distribution obtained from RANS results in the midplane of the REV. $Re_p = 5000$, $\Delta T = 30\text{K}$ (a) $\varphi = 0.600$ (b) $\varphi = 0.650$ and (c) $\varphi = 0.717$.

As reported by Srikanth et al. [44], a symmetry breaking phenomenon is shown to occur in turbulent flow in porous media with low porosity. After the symmetry breaking occurs, the macroscopic flow deviates from the direction in which the pressure gradient is applied, forming a

macroscopic flow angle $\langle\theta\rangle^i$, which is defined as the angle between the direction of the applied pressure gradient and the volume average flow direction. The variation of macroscopic flow angle $\langle\theta\rangle^i$ with porosity is shown in

Figure 3.1. This phenomenon results in different vortex patterns forming in the porous medium flow as $\langle\theta\rangle^i$ varies, as shown in **Figure 3.2**. The magnitude of the deviation is strongly influenced by the porosity of the porous medium. As the porosity decreases from unity, the macroscopic flow angle $\langle\theta\rangle^i$ increases.

The macroscopic flow angle exhibits a sudden increase as the porosity decreases from 0.65 to 0.6, then slightly increases as the porosity decreases further. At higher porosities ($\varphi > 0.800$), the average flow direction generally stays in the same direction of applied pressure gradient ($\langle\theta\rangle^i = 2.3 \times 10^{-5}$). As the porosity decreases ($0.497 < \varphi < 0.717$), the direction of the average flow starts to deviate from the direction of applied pressure gradient. In this range of porosity, the shape of the wake behind each obstacle changes with respect to the change in the macroscopic flow angle. The vortices inside the wake are regions with a low velocity that form an insulating layer on the surface of the obstacles, affecting heat transfer from the area of contact between the vortices in the wake and the surface of an obstacle (A_{vc}). A_{vc} is defined as

$$A_{vc} = \frac{A_{wake}}{A_{total}} \tag{3.2}$$

where A_{wake} is the area of the wake in contact with the obstacle (between the two separation points on the obstacle) and A_{total} is the total surface area of the obstacle. The increase in the macroscopic flow angle leads to a decrease in A_{vc}.

Due to the nature of the flow interaction with the obstacle walls, larger vortices are formed during the transition between minimum to maximum deviation, which leads to a decrease in the heat transfer rate during the transition. Once the deviation of the flow from the direction in which the pressure gradient is applied reaches its highest value, the vortex separation point on one side of the obstacle is pushed downstream, resulting in the contact area between the vortices and the obstacle surface to decrease. Consequently, the heat transfer rate increases. The heat transfer rate at maximum deviation, having a smaller contact area A_{vc}, is higher than that for the case with zero deviation, showing that the observed phenomenon can help to increase the rate of heat transfer in porous media under certain conditions. The corresponding macroscopic flow angle, $\langle\theta\rangle^i$, and contact area between the wake and obstacle, A_{vc}, for various values of porosity, φ, are shown in **Table 3.1**.

The correlation of the average heat flux on the surfaces of the obstacles in the REV (q_{avg}) and the contact area between the wake vortices and the obstacle surface (A_{vc}) is shown in

Figure 3.3. The heat flux, q_{avg}, increases as the contact area, A_{vc}, decreases. We anticipate that q_{avg} reaches an upper limit as A_{vc} decreases to zero. This result supports our hypothesis that the vortices are regions with low velocity that form an insulating layer on the surface of the obstacles.

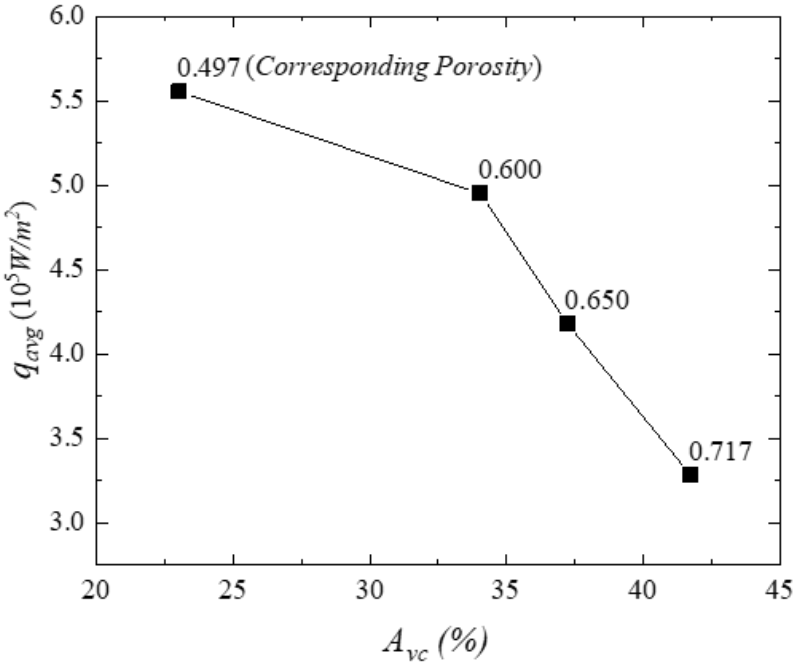

Figure 3.3 Correlation between the average heat flux on surfaces of the obstacles in the REV (q_{avg}) and the contact area between the wake vortices and the obstacle surface (A_{vc}). The corresponding porosity is labeled for each data point.

Table 3.1 Macroscopic flow angle, $\langle\theta\rangle^i$, and contact area between the wake and obstacle, A_{vc}, for various values of porosity, φ.

φ	.497	.600	.650	.717
$\langle\theta\rangle^i$	3.63°	9.81°	6.63°	1.82°
A_{vc}	.230	.340	.372	.417

There are two main vortices forming in the wake of each obstacle, with the top vortex being slightly smaller than the bottom vortex. To measure the size of the top and bottom vortices in the wake, we define the non-dimensional Vortex Core diameter, d_v, as follows. Drawing a straight line between the top and bottom vortex cores (located using the maximum vorticity magnitude), there is a point of minimum vorticity, $P_{contact}$, on this line. $P_{contact}$ corresponds to a location where the top and bottom vortices are in contact. The vortex radius is defined as the distance between the vortex core and $P_{contact}$. The obstacle diameter is used to non-dimensionalize the Vortex Core diameter. The variation of d_v with porosity is shown in **Figure 3.4**.

The size of the vortices, measured by d_v, stays relatively constant for $\varphi < 0.600$ and increases with the increase of porosity between $0.600 < \varphi < 0.717$. The ratio of the diameters of the top and bottom vortices is independent of the value of porosity for $0.600 < \varphi < 0.717$. For $\varphi > 0.800$, the average flow direction does not deviate from the driving force direction and the sizes of the top and bottom vortices become equal. More investigation is needed to verify the relation between the porosity and vortices inside the wake.

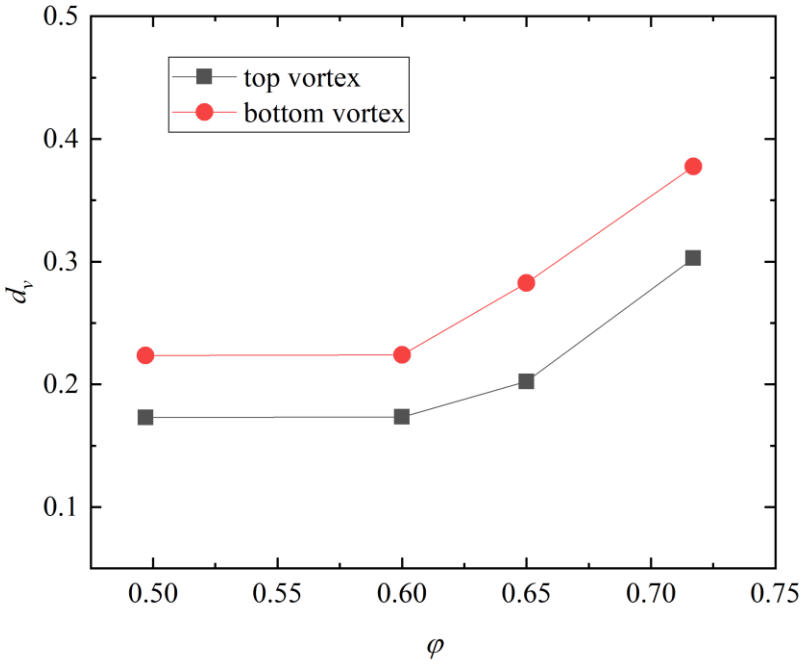

Figure 3.4 Variation of the Vortex Core Diameter, d_v, of the top and bottom vortices in the wake versus porosity, φ.

3.3.2 Obstacle Shape

Different shapes of obstacles composing a porous medium result in different flow patterns in a porous media flow, with flow separation happening on sharper edges of the obstacle wall. Under the conditions of $\varphi = 0.497$, $Re_p = 5000$, and $\Delta T = 30\text{K}$, the results for two homogeneous porous media consisting of either circular or square cylinders are vastly different. The streamlines and temperature distributions for these two cases are shown in **Figure 3.5**.

The case of a porous medium composed of circular cylinders has two vortices in the wake of each cylinder that are attached to the obstacle surface, with a contact area $A_{vc} = 23\%$ and the average heat flux $q_{avg} = 5.554 \times 10^5 \ W/m^2$, as shown in **Figure 3.5** (a). In the case of

a porous medium comprised of square cylinders, a square obstacle is in contact with four vortices, located in the gaps between the upstream and downstream obstacles, as shown in **Figure 3.5** (b). The vortices for the square obstacle case form a flow similar to that of a lid driven cavity, with a total contact area on an obstacle of $A_{vc} = 50\%$, and the average heat flux of $q_{avg} = 4.723 \times 10^5\ W/m^2$. In the case of cylindrical obstacles, the primary flow in the porous medium weaves around the obstacles. As our hypothesis suggests, the size of the contact area between the vortices and the obstacle surface, A_{vc}, correlates with the heat transfer between the obstacles and porous media flow.

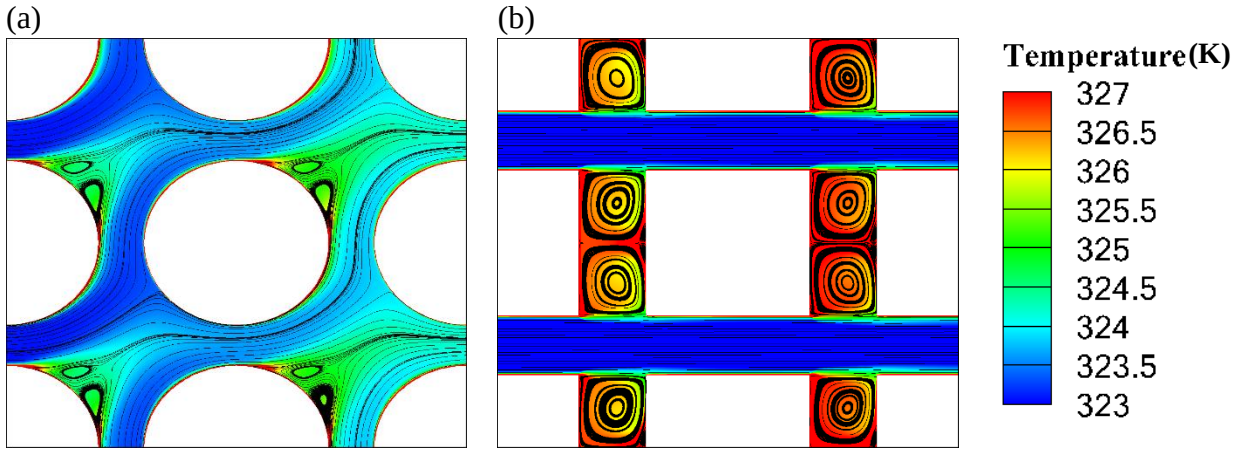

Figure 3.5 Streamlines and the temperature distribution obtained from RANS results in the midplane. Porous media flow in (a) A porous medium comprised of circular cylinders, (b) A porous medium comprised of square cylinders. $\varphi = 0.497$ and $Re_p = 5000$.

3.3.3 Reynolds Number

At low Reynolds numbers ($Re_p < \sim 100$) in the laminar flow regime, the phenomenon of flow deviation from the direction of the applied pressure gradient does not occur, and the flow

remains parallel to the direction of the pressure gradient. This forms large vortices between neighboring obstacles in the *x*-direction. As the flow transitions from laminar to turbulent somewhere between $50 < Re_p < 500$, the flow pattern changes with the change of the Reynolds number, resulting in smaller vortices attached to the obstacles as the macroscopic flow angle, $\langle\theta\rangle^i$, deviates from zero. Our numerical finding that the flow transition happens between $50 < Re_p < 500$ is supported by de Lemos [18] and Kaviany [45], who stated that flow in porous media is fully turbulent at $Re_p = 300$.

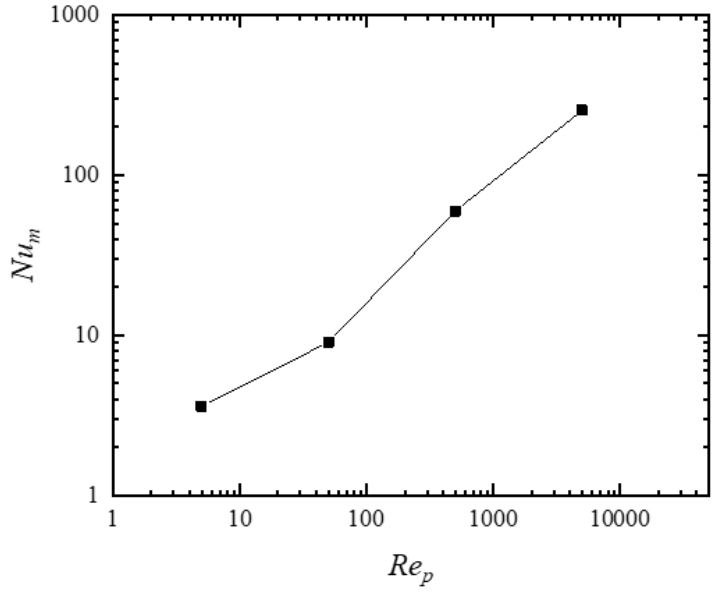

Figure 3.6 Correlation between the Pore Scale Reynolds number Re_p and mean Nusselt number Nu_m on the top left obstacle in the REV.

Although our hypothesis states that the areas of the obstacle surface in contact with wake vortices will have a lower heat transfer rate compared to the areas in contact with the primary

flow, the effect of this is small compared to the effect of the Reynolds number, Re_p, on the overall heat flux, q_{avg}. The correlation between the Pore Scale Reynolds number, Re_p, and the mean Nusselt number, Nu_m, of an obstacle is shown in

Figure 3.6. The slight change of the correlation between Re_p and Nu_m between ($50 < Re_p < 500$) is likely due to the wake developing into a complex three-dimensional flow in this flow regime.

Table 3.2 Comparison of RANS and time averaged LES results at $\varphi = 0.497$ and $Re_p = 500$. Here $u_{m,x}$ and $u_{m,y}$ are the mean velocity in the *x*-and *y*-directions respectively, and $\langle\theta\rangle^i$ is the macroscopic flow angle, defined as $\tan^{-1}(u_{m,y}/u_{m,x})$.

	RANS	LES(time averaged)
$\langle\theta\rangle^i$	32.903°	32.875°
$u_{m,x}$	0.1258	0.1296
$u_{m,y}$	0.0814	0.0837
Nu_m	59.953	72.650

An LES simulation was performed for $\varphi = 0.497$ and $Re_p = 500$. The time averaged LES solution in the REV mid-plane is shown in

Figure 3.7. A comparison between the RANS and LES solutions is shown in **Table 3.2**. The difference between the Nu_m of the RANS and LES cases are caused by the vortex shedding off the obstacle walls in the LES case, which is absent in the steady RANS simulation. Energy "packages" are delivered from the obstacle wall to the primary flow as the vortices are shed off the wall. This mechanism enhances heat exchange between the obstacle wall and the primary

flow. This phenomenon is responsible for the higher Nu_m for the LES case compared to the RANS case (**Table 3.2**).

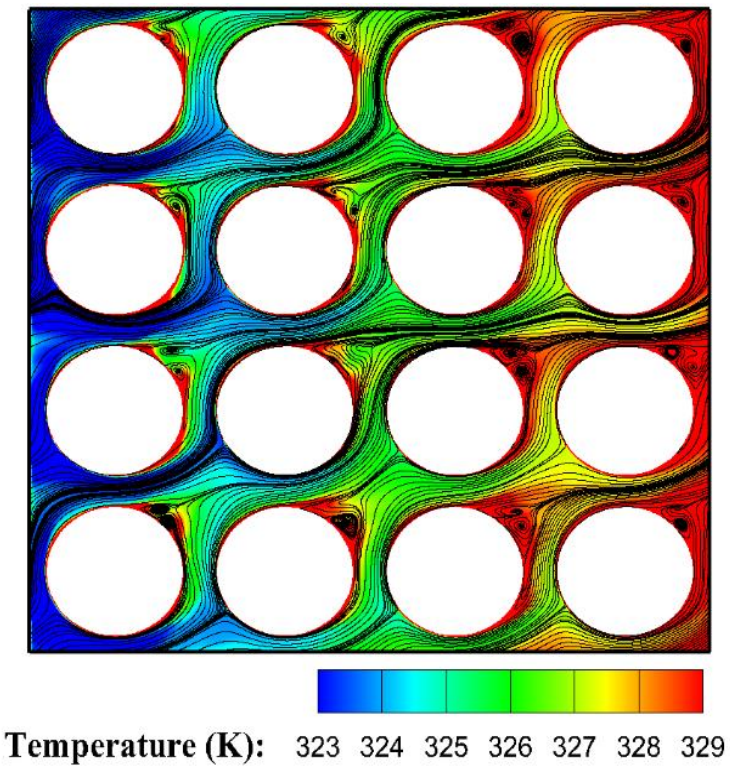

Figure 3.7 Streamlines and temperature distribution obtained from time averaged LES results in the midplane of the REV. $Re_p = 500$, $\Delta T = 30$K, and $\varphi = 0.497$.

3.4 Conclusions

The results of our simulations support the hypothesis that the rate of heat transfer between the obstacle surface and the fluid is influenced by the size of the contact area of the vortices that are attached to the solid obstacles in the porous medium. The phenomenon of flow deviation from the driving force direction is shown to help increase the rate of heat transfer in porous media under certain conditions.

Although the contact area between the vortices and the obstacle surface, A_{vc}, has a considerable effect on the overall heat transfer from the obstacle to the fluid, it is not as significant compared to the effect of the Pore Scale Reynolds number Re_p. However, in practice, increasing the Reynolds number requires using a larger applied pressure gradient to drive the flow faster. Our results show that by manipulating the vortex contact area with the obstacle by modifying such parameters as the obstacle shape or porosity while keeping the Reynolds number the same, the overall heat transfer rate between the obstacles and fluid can be increased in an "economical" way, without increasing the applied pressure gradient.

More DNS and LES studies are needed to gain a further understanding into the effect of turbulent vortices on heat transfer in porous media.

CHAPTER 4

Microscale Turbulent Structures Dynamics on Forced Convection

4.1 Abstract

From the previous chapter, we have established the importance of the influence of microscale flow structures (smaller than the pore size) on turbulent heat transfer in porous media. Yet the error between RANS and LES results lead us to believe that there are time dependent effects within the porous media flow that have significant importance to heat convection.

The goal of this study is to determine these effects and their influence of the micro-vortices on convection heat transfer in turbulent porous media flow. Turbulent flow in a homogeneous porous medium was investigated using Large Eddy Simulation (LES) at a Reynolds number of 300. The study has been performed for obstacles with shapes of square and circular cylinders at porosities of 0.50 and 0.87. We observed that the convection heat transfer characteristics are dependent on whether the micro-vortices are attached or detached from the surface of the obstacle. There is a spectral correlation between the Nusselt number and the pressure instabilities due to vortex shedding.

For porosity of 0.50, we observe dominant frequencies in the spectrum plot of the drag coefficient that correspond to vortex shedding and a secondary flow instability. For the porosity of 0.87, the frequencies of the drag coefficient are distributed across the spectrum. The secondary flow instability occurs due to high pressure regions forming periodically near the converging pathway between obstacles. This causes local adverse pressure gradient, affecting the flow velocity and convection heat transfer. We also observe a phase difference between the vortex shedding process of each obstacle. Depending on the phase difference in the vortex dynamics between each obstacle,

the amplitude of the shedding vortices will experience constructive or destructive interference. Understanding the dominant modes that affect convection heat transfer can aid in finding an optimum geometry for the porous medium.

4.2 Introduction

Models of turbulent porous media flow are useful for the systematic study for applications such as canopy flows, pebble bed nuclear reactors, heat exchangers, porous chemical reactors, and crude oil extraction [17]. From the previous chapters, we have established the importance of microscale flow structures (smaller than the pore size) on convection heat transfer in porous media flow. Modeling the effects of the microscale flow structures needs a systematic study on these microscopic flow mechanics [16].

In this chapter, we attempt to identify and understand the important mechanisms of the micro-vortices that influence convection heat transfer in turbulent porous media flow. Macroscopic turbulence models for porous media flows have been developed throughout the years [18–21], combining the Volume Average Theory (VAT) [22] with Reynolds Averaging (RA). Reynolds Averaged Navier-Stokes (RANS) simulations of microscale porous media flow have been used to determine coefficients for the RA-VAT models [23–25]. However, the results from microscale RANS simulations are constrained by the modelling error [26].

Jin et al. [27] and Uth et al. [28] performed Direct Numerical Simulation (DNS) of forced convection flows in porous media, which suggested that the pore size of the porous medium determines the maximum size of turbulent eddies. The study led to the development of a mixing-length macroscale model based on the mixing layer hypothesis by Jin & Kuznetsov [29]. DNS studies by He et al. [30] verified that the turbulence integral length scale is ~10% of the obstacle

diameter in a closely packed porous medium. Turbulent energy transport is crucial for studying convection heat transfer in porous media. Several macroscopic energy models have been developed that make use of the gradient diffusion hypothesis in conjunction with the assumption of thermal equilibrium between the solid and fluid phases [25], [31].

Microscale studies show that the heat transfer efficiency between the obstacle surface and the fluid increases with an increase in the Reynolds number and obstacle diameter [32,33]. The microscale simulations for square rods [31], circular rods [34], and elliptic rods [35] revealed that the thermal dispersion varies drastically with the obstacle shape. The functional dependence of the Nusselt number on porosity changes with the obstacle shape [36]. High Resolution LES studies of finite pebble beds show that hot spots appear on the surface of the pebbles are highly unsteady, in which their locations move over time [37], highlighting the importance of a transient analysis. The microscale distribution of the Nusselt number from DNS studies [32] shows that the unsteady wake region contributes the least towards heat transfer. Turbulent thermal mixing for circular rods increases with an increase in the Reynolds number and approaches an asymptotic value at higher Reynolds numbers [38].

4.3 Methods

4.3.1 Simulation Conditions

REVs with $4s \times 4s \times 2s$ similar to the arrangement in **Figure 1.1** were used for investigation. We use cases with $2s \times 2s \times 2s$ REV for grid study; all simulation cases are listed in **Table 4.1**. Periodic boundary conditions are used to impose an infinite span in all directions to avoid finite boundary effects. The phenomena that are observed inside the periodic domain can thus be linked to the porous medium alone. Two values of porosity (φ) are studied, 0.50 and

0.87, while the Pore Scale Reynolds number (Re_p) is 300 unless specified otherwise. The Re_p was maintained using a constant applied pressure gradient (dp/dx) as the driving force. These parameters are defined in equations (1.1) and (1.2).

where d is the diameter of cylindrical obstacles, u_m is the mean velocity in the x-direction, and ν is the kinematic viscosity of the fluid. The temperature of the walls of the cylindrical obstacles was set to a constant value of 353K, while the average temperature of the inlet flow was set to 323K. With this boundary condition setting, the characteristic temperature difference, ΔT, was 30K. The Prandtl number (Pr) was kept constant at 6.99. We use RANS and LES methods to simulate the microscopic flow field. The Dynamic One-equation TKE (DOTKE) subgrid model has been used for LES. Simulations were performed using the commercial CFD code ANSYS Fluent 16.0.

Table 4.1 The cases with $4s \times 4s \times 2s$ REVs (A1-A3), simulated for investigation of heat convection. The cases with $2s \times 2s \times 2s$ REVs (B1-B9), for energy spectrum and grid quality assessment.

Case ID	Obstacle Shape	Porosity	Grid Resolution, $\Delta x_{max}/s$= 0.05
A1	Circular	0.50	0.0250
A2	Circular	0.87	0.0250
A3	Square	0.87	0.0250
B1	Circular	0.50	0.0500
B2	Circular	0.50	0.0250
B3	Circular	0.50	0.0125
B4	Circular	0.87	0.0500
B5	Circular	0.87	0.0250
B6	Circular	0.87	0.0125
B7	Square	0.87	0.0500
B8	Square	0.87	0.0250
B9	Square	0.87	0.0125

4.3.2 Numerical Methods

Equations (4.1)-(4.2) show the filtered Navier-Stokes equations, the tilde notation (⧈̃) denotes spatial filtering. The filtered Navier-Stokes equations are solved in conjunction with the DOETKE subgrid model using the Finite Volume Method (FVM). A box filter is implicitly applied by the computational grid in the FVM. The pressure term $\tilde{p}$ here is a filtered periodic pressure. The subgrid velocity scale is estimated by solving a transport equation for the subgrid turbulence kinetic energy k_{SGS} (equation (4.3)). The subgrid length scale Δ is set as the cube root of the cell volume. Equation (4.4) estimates the subgrid turbulence eddy viscosity. The model constants C_k and C_ε are determined by the localized dynamic subgrid-scale model from [46]. We are filtering the grid scale velocity field to a test scale velocity field. The test filter length $\hat{\Delta}$is equal to twice the grid filter length Δ. We invoke the similarities between the stresses at the two scales to determine the model constants. Model constant C_k is determined in equations (4.5)-(4.6) by using the similarity between the SGS stress tensor τ_{ij} and the test Leonard stress tensor L_{ij}. The value of C_k is controlled by $-\mu/\left({k_{SGS}}^{1/2}\Delta\right)$. Model constant C_ε is determined in equation (4.7) by using the similarity between the dissipation rate at the grid level ε_{SGS} and the test level ε_{test}.

$$\frac{\partial \widetilde{u_j}}{\partial x_j} = 0 \tag{4.1}$$

$$\frac{\partial \rho \widetilde{u_\iota}}{\partial t} + \frac{\partial \rho \widetilde{u_\iota}\widetilde{u_j}}{\partial x_j} = -\frac{\partial \tilde{p}}{\partial x_i} + \frac{\partial}{\partial x_j}\left[(\mu + \mu_{T,SGS})\left(\frac{\partial \widetilde{u_\iota}}{\partial x_j} + \frac{\partial \widetilde{u_j}}{\partial x_i}\right)\right] + \rho g_i \tag{4.2}$$

$$\frac{\partial k_{SGS}}{\partial t} + \frac{\partial\left(\widetilde{u_j} k_{SGS}\right)}{\partial x_j} = \left[C_k k_{SGS}^{1/2}\Delta\left(\frac{\partial \widetilde{u_\iota}}{\partial x_j} + \frac{\partial \widetilde{u_j}}{\partial x_i}\right)\right]\frac{\partial \widetilde{u_\iota}}{\partial x_j} - C_\varepsilon \frac{k_{SGS}^{3/2}}{\Delta} + \frac{\partial}{\partial x_j}(\mu_{T,SGS}\frac{\partial k_{SGS}}{\partial x_j}) \tag{4.3}$$

$$\mu_{T,SGS} = C_k k_{SGS}^{1/2} \Delta \tag{4.4}$$

$$\tau_{ij} = -2C_k k_{SGS}{}^{\frac{1}{2}} \Delta \widetilde{S_{ij}} + \frac{2}{3}\delta_{ij} k_{SGS};\ L_{ij} = -2C_k k_{test}{}^{\frac{1}{2}} \hat{\Delta} \widehat{\widetilde{S_{ij}}} + \frac{1}{3}\delta_{ij} L_{kk} \tag{4.5}$$

$$C_k = \frac{1}{2}\frac{L_{ij}\sigma_{ij}}{\sigma_{ij}\sigma_{ij}};\ \sigma_{ij} = -\hat{\Delta} k_{test}{}^{\frac{1}{2}} \widehat{\widetilde{S_{ij}}};\ k_{test} = \frac{1}{2}\left(\widehat{\widetilde{u_k}\widetilde{u_k}} - \widehat{\widetilde{u_k}}\,\widehat{\widetilde{u_k}}\right) \tag{4.6}$$

$$C_\varepsilon = \frac{\widehat{\left(\partial\widetilde{u_i}/\partial x_j\right)\left(\partial\widetilde{u_i}/\partial x_j\right)} - \left(\partial\widehat{\widetilde{u}_i}/\partial x_j\right)\left(\partial\widehat{\widetilde{u}_i}/\partial x_j\right)}{\left(\left(\mu + \mu_{T,SGS}\right)\hat{\Delta}\right)^{-1} k_{test}{}^{3/2}} \tag{4.7}$$

4.3.3 Grid Resolution

Grid resolutions for LES cases as well as maximum values of non-dimensional near-wall grid spacing, Δy^+_{max}, are shown in **Table 4.2**. The LES Index of Quality (LES_IQ) [47] is used to provide the fraction of the total turbulence kinetic energy that is resolved by the grid. Assuming recommended 80% of the energy resolved in LES [48], the simulated LES_IQ should be greater than 0.8. Remarks from Celik *et al.*[47] indicate that simulations may be considered to be of DNS quality with LES_IQ > 0.9. The volume averaged LES_IQ for all the LES simulations in this work meet this criterion after time averaging. The minimum and spatially averaged values of LES_IQ at an instant in time are reported in **Table 4.3**. For the LES cases, the turbulence kinetic energy spectrum is used to identify the scale regimes of turbulence that have been resolved in this work. The turbulence kinetic energy spectra ($E_{ii}/3$) versus the wavenumber ($k \cdot s$) for the LES test cases are shown in **Figure 4.1**.

Table 4.2 The maximum value of non-dimensional near-wall grid spacing, Δy^+_{max}, measured on the surface of the solid obstacles for the grid resolution test cases. It should be noted that these are small areas with high Δy^+ values, overall Δy^+ values on the obstacle surfaces are kept below 1.

Δy^+_{max}			
Case	Coarse grid, $\Delta x_{max}/s$= 0.05	Intermediate grid, $\Delta x_{max}/s$= 0.025	Fine grid, $\Delta x_{max}/s$= 0.025
A1 ($\varphi = 0.50$)	1.06	1.16	1.05
A2 ($\varphi = 0.87$)	1.68	1.81	1.79
A3 ($\varphi = 0.87$(square))	1.87	1.65	1.79

Table 4.3 The value of LES_IQ measured in the fluid volume for the grid resolution test cases (B1-B9). Both the minimum and the volume-averaged values are reported (ranges from 0 to 1, high values indicate high resolution with a large fraction of the turbulence kinetic energy being resolved).

LES_IQ				
Porosity φ		Coarse grid, $\Delta x_{max}/s$= 0.05	Intermediate grid, $\Delta x_{max}/s$= 0.025	Fine grid, $\Delta x_{max}/s$= 0.0125
0.50	minimum	0.22	0.44	0.66
	average	0.81	0.95	0.98
0.87	minimum	0.70	0.73	0.80
	average	0.96	0.98	0.99
0.87(square)	minimum	0.69	0.74	0.89
	average	0.95	0.98	0.99

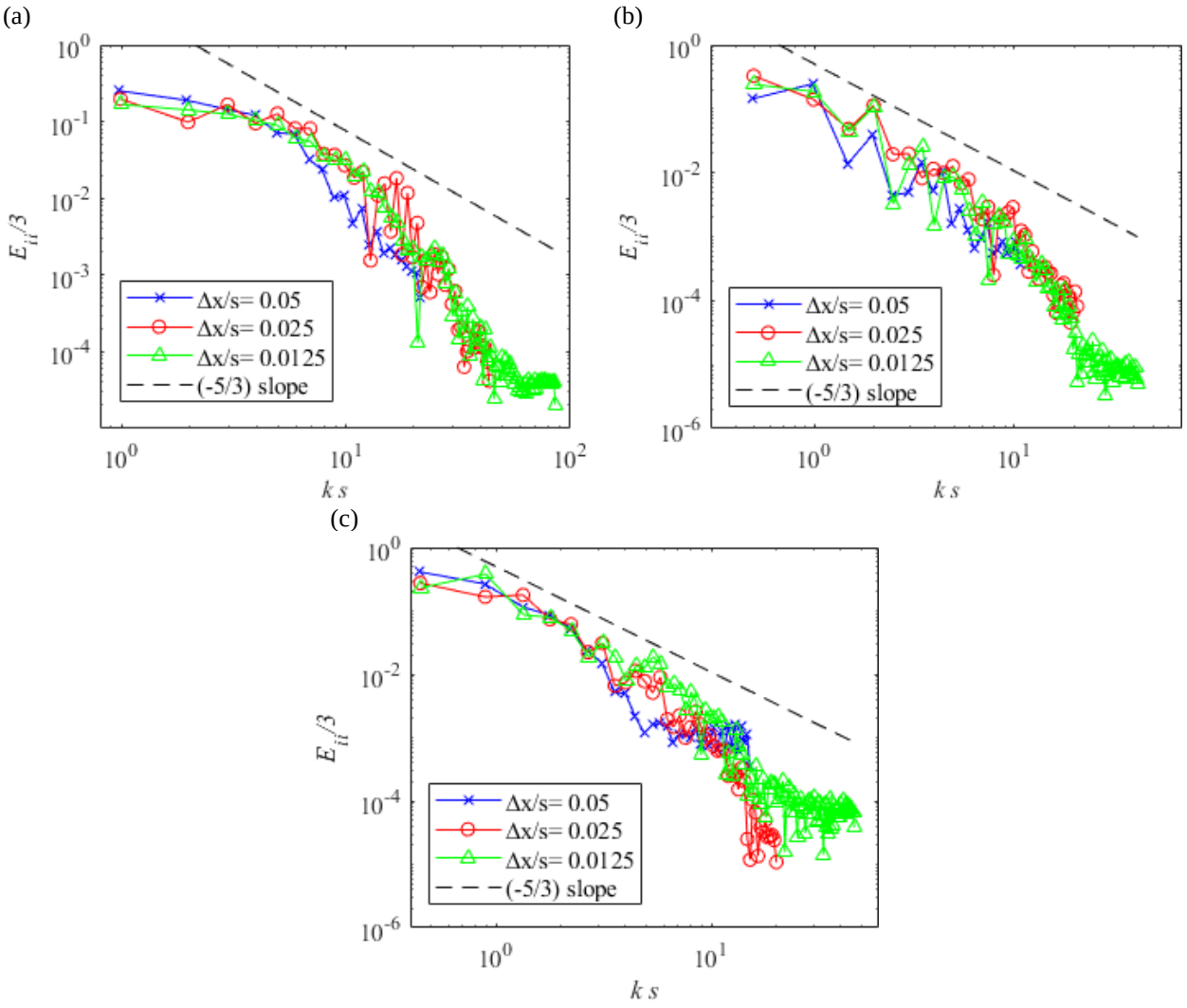

Figure 4.1 Turbulence energy spectrum for LES cases (a) $\varphi = 0.50$ with circular obstacles; (b) $\varphi = 0.87$ with circular obstacles; (c) $\varphi = 0.87$ with square obstacles. The dashed line corresponds to the -5/3 slope on the log plot.

4.3.4 Importance of Time Dependent Effects

Heat transfer in porous media is closely linked to the formation, propagation, and dissipation of flow structures. The use of RANS simulations to determine coefficients for the RA-VAT models will not accurately capture time dependent effects such as vortex shedding or Hopf bifurcations in periodic porous media, which leads to a considerable error when using

them. The temperature fluctuation for case A1 is shown in **Figure 4.2**. The temperature fluctuations, with the intensity that ranges ~15% for case A1, come from vortex shedding and flow instabilities (discussed in sections 4.4.1, 4.4.3 and 4.4.4). It is reasonable to assume the importance of these time dependent effects when considering heat transfer simulations.

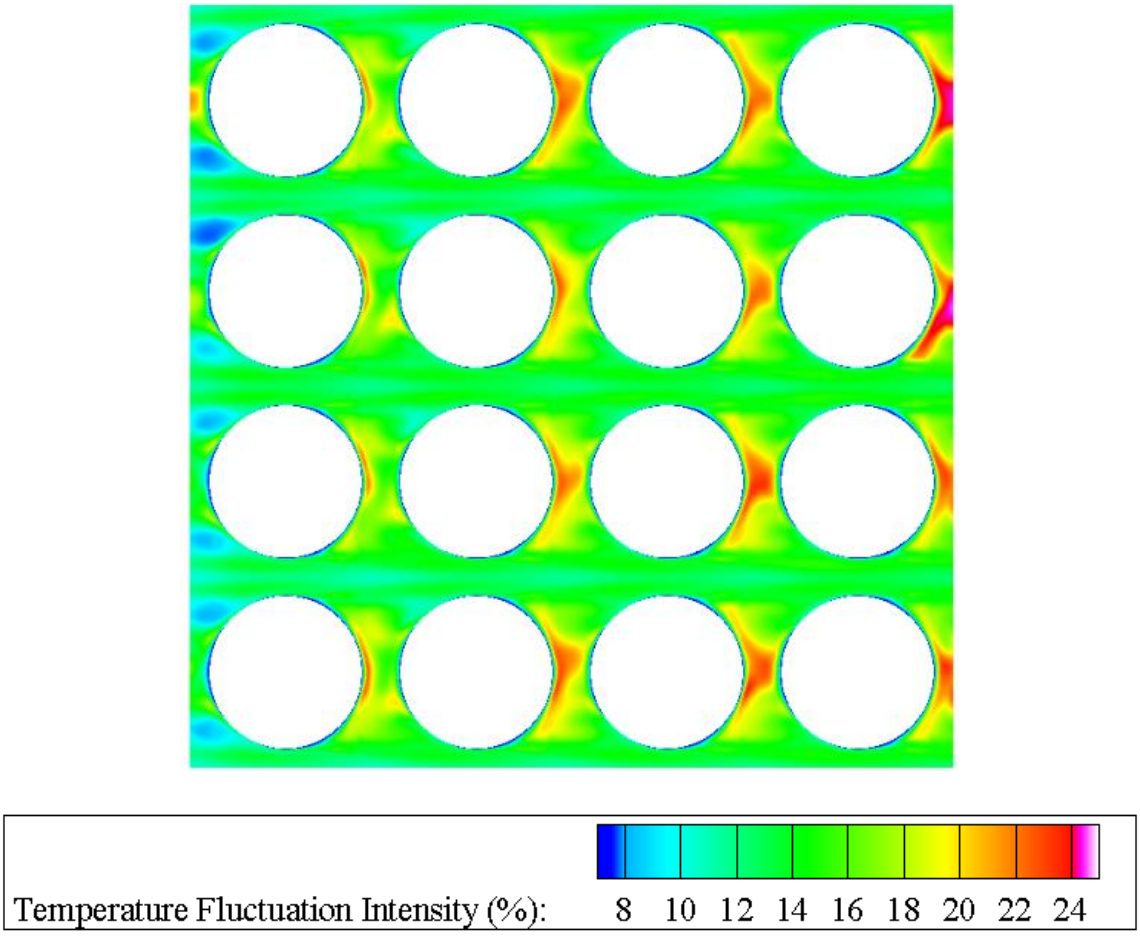

Figure 4.2 The temperature fluctuation as percentage of temperature difference between obstacle surface and average inlet temperatures ($\Delta T = 30$K). LES case $\varphi = 0.50$ and $Re_p = 300$.

4.4 Results and Discussion

4.4.1 Flow Instability

For $Re_p = 300$, the von Kármán instability is observed for the flow around each obstacle. The amplitude of lift oscillation from the von Kármán instability depends on the obstacle shapes as well as porosity (φ). A symmetry-breaking flow bifurcation is expected to occur at this Re_p. The mean flow direction of the porous medium flow can either coincide with the driving force or deviate from the direction of the driving force. The phenomenon originates from asymmetrical vortex breakdown and it is highly sensitive to the geometry of the porous medium. The formation of flow deviation has been studied in detail by Srikanth *et al*. [49]. The deviating direction around the flow of each cylinder is synced for obstacles in the same column, where any sway from the sync will be corrected by the neighboring obstacle flow of the same column. **Figure 4.3** illustrates the lift coefficient (C_l) over time for the case of $Re_p = 300$, $\varphi = 0.87$ with circular cylinder obstacles (case A2). Only the 1st column of obstacles in the REV are plotted to avoid the figure becoming too busy. The direction of flow deviation can be observed from the C_l oscillation over time. **Figure 4.4** (b) illustrates a snapshot of this case, where C_l is at a positive value for the 1st column of obstacles. The existence of this phenomenon highlights the importance of micro-vortices in transport in porous media, since it is a source of enhanced flow mixing. Different geometries will have different flow features due to the interaction of the micro-vortices with the surfaces of the obstacles forming the porous medium.

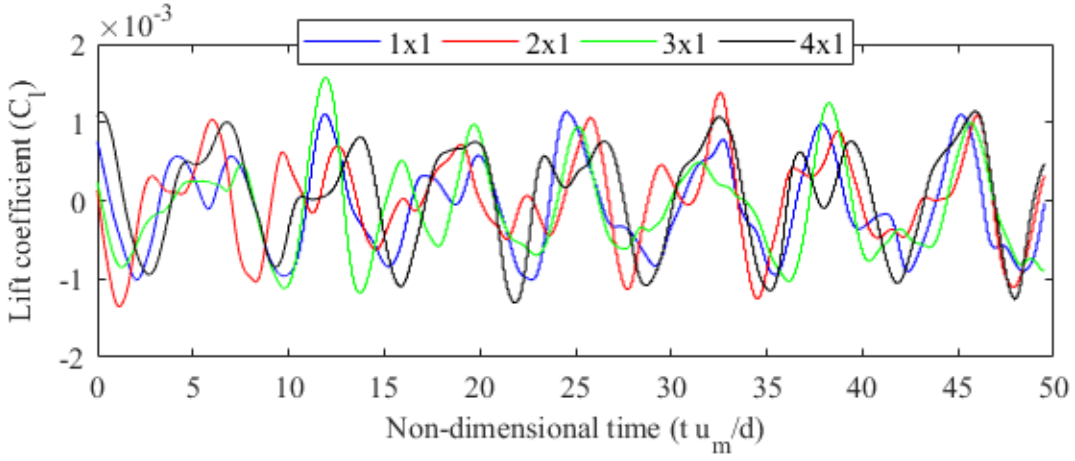

Figure 4.3 Change of lift coefficient (C_l) over time for obstacles in the 1st column for case A2 ($Re_p = 300$, $\varphi = 0.87$ with circular cylinder obstacles).

4.4.2 Recirculating and Shedding Vortices

The micro-vortices that are generated behind the solid obstacle are pockets of slow-moving fluid, which insulate the solid obstacle from the fast-moving fluid. This reduces the effective surface area that is available for heat transfer. For the circular cylinder obstacles, a more diffuse temperature distribution is observed in a shedding vortex system. A shedding vortex system will perform the additional role of carrying away pockets of heat from the obstacle surface. If the amplitude from the von Kármán instability is not sufficient for the wake vortices to break into the primary duct flow, a recirculating vortex system is formed between two neighboring obstacles in the same row. This is illustrated in case A1 (**Figure 4.4** (a) and **Figure 4.5**). The recirculating vortex system traps heat in the streamwise pore space rendering the vortex-covered portion of the surface area less conducive for heat removal. On the other hand, if the wake vortices can break into the primary flow, vortices will periodically form near the obstacle surface and carry heat when dissipated into the primary flow, as illustrated in case A2

(**Figure 4.4** (b) and **Figure 4.6**). The temperature distribution in this case will have steep gradients, which increases the surface heat transfer rate. A similar behavior can be found in case A3 (**Figure 4.4**(c) and **Figure 4.7**), where the obstacles are square cylinders. The wake vortices can break into the primary flow, but due to the sharp corners of the square obstacle shape, the location of the separation points does not change over time. This results in a smaller amplitude of intensity when vortices periodically form and dissipate, as well as a constant contact area between the wake vortices and the obstacle surface.

(a) Case A1

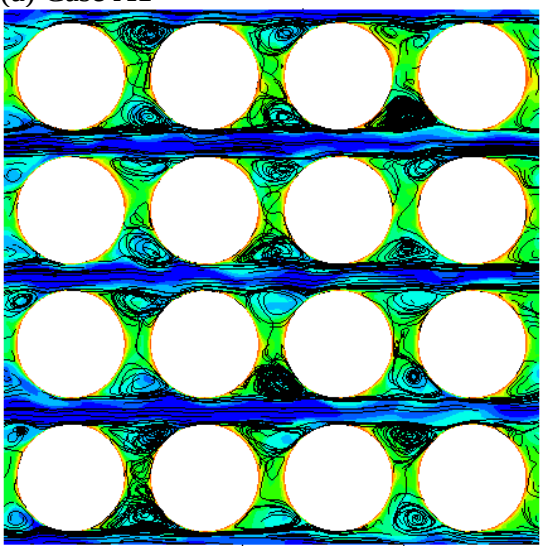

(b) Case A2

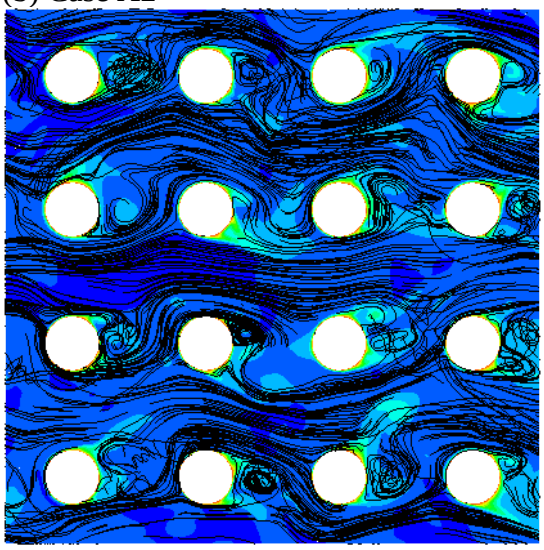

(c) Case A3

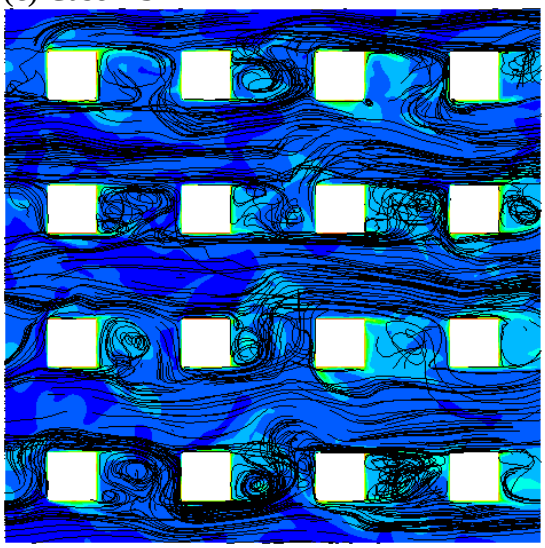

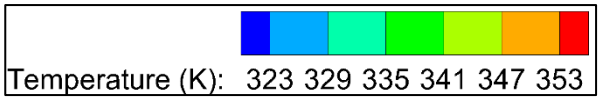

Case ID	Obstacle Shape	Porosity	Type
A1	Circular	0.50	LES
A2	Circular	0.87	LES
A3	Square	0.87	LES

Figure 4.4 Streamlines and temperature distribution in a porous medium consisting cylindrical obstacles with porosity of (a) Case A1, $\varphi = 0.50$ with circular obstacles; (b) Case A2, $\varphi = 0.87$ with circular obstacles; (c) Case A3, $\varphi = 0.87$ with square obstacles.

The main difference in terms of vortex shedding for these cases is that for case A1, the vortex is shed into with the dissipating vortex that was previously shed, while in case A2 and A3 the vortices are shed directly into the primary flow. The space between the obstacles (porosity) is the cause for this difference in vortex shedding. Two distinct momentum transport processes,

micro-vortex transport from the surface and turbulent mixing in the bulk flow, govern heat transfer inside porous media. The dominance of each process is observed to be sensitive to the geometry of the porous medium and the Reynolds number of the flow.

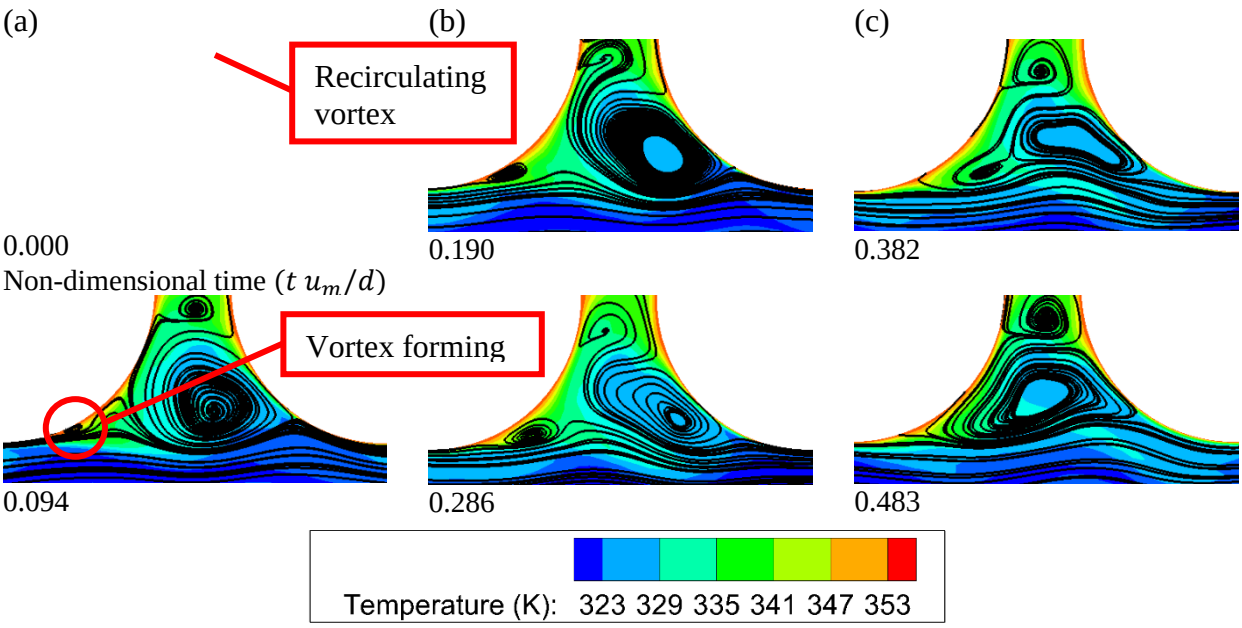

Figure 4.5 Example of vortex shedding and its contribution to heat transfer from case A1 (a) A vortex that begins to form while the previous vortex is combined with the recirculating vortex. (b) A developed vortex that acts as an insulation layer on the obstacle surface. (c) The vortex is shed from the obstacle surface, then combined with the dissipating vortex that was previously shed. A new vortex starts forming.

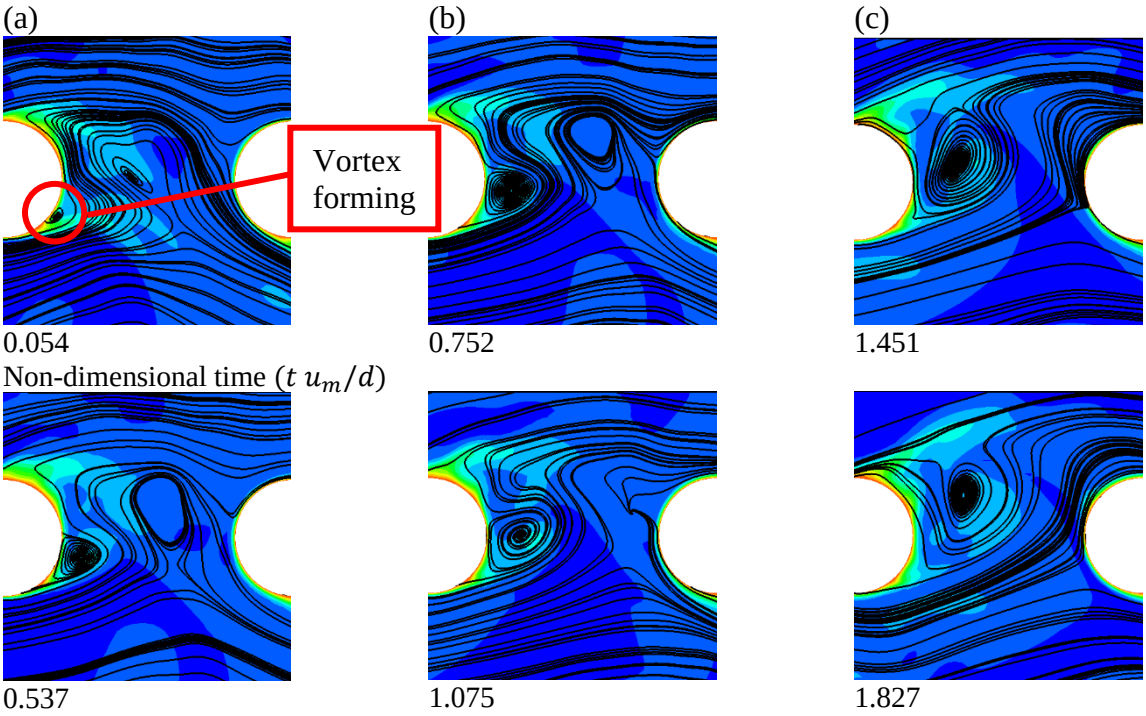

Figure 4.6 Example of vortex shedding and its contribution to heat transfer from case A2 (a) Vortex beginning to form while the previous vortex is shed and dissipated downstream. (b) A developed vortex that acts as an insulation on the obstacle surface. (c) Vortex is shed downstream, a new vortex starts forming.

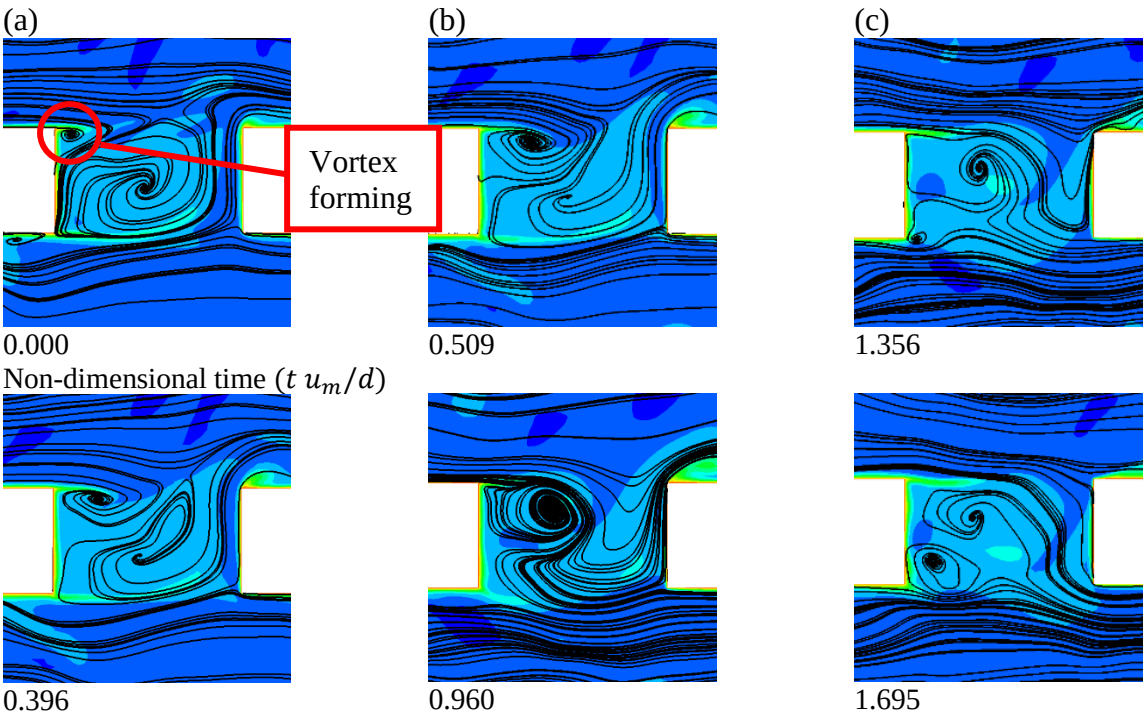

Figure 4.7 Example of vortex shedding and its contribution to heat transfer from case A3. (a) Vortex beginning to form while the previous vortex occupies the space between obstacles. (b) A developed vortex that acts as an insulation on the obstacle surface, pushing out the previous vortex as it grows in size. (c) Vortex has pushed the previous vortex out of the space between obstacles. A new vortex is formed and starts growing.

Convection heat transfer is mainly affected by the following behaviors of the micro-vortices: vortex recirculation, vortex shedding and flow stagnation. Of these three, flow stagnation will also affect the intensity of vortex shedding in addition to its own effect on heat transfer. The recirculating vortices mainly act as an "insulation" region when in contact with the obstacle surface, with a lower convection heat transfer in this region. This is due to a lower velocity and smaller temperature gradient in the recirculating vortices, as shown in **Figure 4.4** (a) and **Figure 4.5**. They are attached to the wake region of the porous medium obstacles.

The shedding micro-vortices transport heat away from the surface and dissipate it in the primary flow. The vortex shedding process starts by vortex formation on the obstacle surface.

Because of the higher temperature gradient and mixing from the newly formed vortex, the surface in contact with the vortex has a higher heat transfer rate at this stage. After the vortex is formed, it grows while being attached to the surface. The vortex acts as an insulation on the obstacle surface in this stage, similar to that of a recirculating vortex. When the vortex is too large to maintain stability on the obstacle surface, it is shed downstream, and a new vortex starts forming. This process is shown in **Figure 4.5**, **Figure 4.6** and **Figure 4.7**.

4.4.3 Flow Instabilities and Vortex Shedding

Flow stagnation happens due to high pressure regions forming periodically near the converging pathway between two obstacles. This is caused by stagnation pressure oscillation caused by competition between the pressure and inertial forces, as shown in **Figure 4.8** (a). The forces are labeled in the macroscale momentum conservation equation (4.8) (de Lemos 2006). The operator $\langle - \rangle^i$ indicates volume average in the fluid domain. ΔV is the volume of the REV, A_i is the interfacial area and n_i is the normal vector of A_i. The vortices that shed periodically from the obstacle surface are similar to that of a von Karman vortex, which introduces oscillations to the forces acting on the obstacle surface. The intensity of the vortex shedding is monitored using the drag forces, which consist of viscous and pressure drag components (equation (4.8)). The pressure drag has a higher magnitude and is therefore more dominant than the viscous drag (**Figure 4.8** (a)).

$$\underbrace{\rho \frac{\partial}{\partial t}\left(\varphi \langle u_i \rangle^i\right)}_{inertial} = \underbrace{\rho \varphi g_i}_{applied} + \underbrace{\frac{\mu}{\Delta V}\int_{A_i} n_j \, \partial_j u_i \, dS}_{viscous\ drag} - \underbrace{\frac{1}{\Delta V}\int_{A_i} n_i p \, dS}_{pressure\ drag} \tag{4.8}$$

To compare the vortex shedding between cases A1, A2, and A3, the standardized pressure drag is defined as equations (4.9)-(4.10) and plotted in **Figure 4.8** (b). The first higher frequency oscillations of the pressure drag represent vortex shedding on the obstacle surface. This is verified by matching the vortex shedding visualization using animation in the format of **Figure 4.5**, **Figure 4.6** and **Figure 4.7** to the oscillation of the pressure drag. The secondary lower frequencies of the pressure drag represent the effect of flow stagnation. To separate the different frequencies in the signal, a Fast Fourier Transform (FFT) is performed on the Drag Coefficient (C_d) and discussed in the next section.

$$Standardized\ pressure\ = (p\ -\ p_{mean})\ /\ p_{std} \tag{4.9}$$

$$Standard\ deviation\ of\ pressure\ (p_{std}) = \sqrt{\sum (p - p_{mean})^2\ /(N-1)} \tag{4.10}$$

We also observe a phase difference between the vortex shedding process of each obstacle. Depending on the timing of the vortex shedding process between each obstacle, the amplitude of the shedding vortices will experience constructive or destructive interference. We can see this from the standardized pressure force signals in **Figure 4.8** (b), where the signals of the standardized pressure forces for case A1 and A2 show constructive or destructive interference over time. This effect is not as prominent in case A3, which either means the vortex shedding are in sync throughout the REV domain or the effect of vortex shedding for each obstacle does not interfere with the vortex shedding on other obstacles. From visualization of the flow field streamlines, the latter seems to be the case. There is a phase difference between the vortex shedding process of each obstacle, but the porous medium geometry of square obstacles

restricts the vortex shedding locations, constraining the of vortex shedding process to be mostly independent for each obstacle.

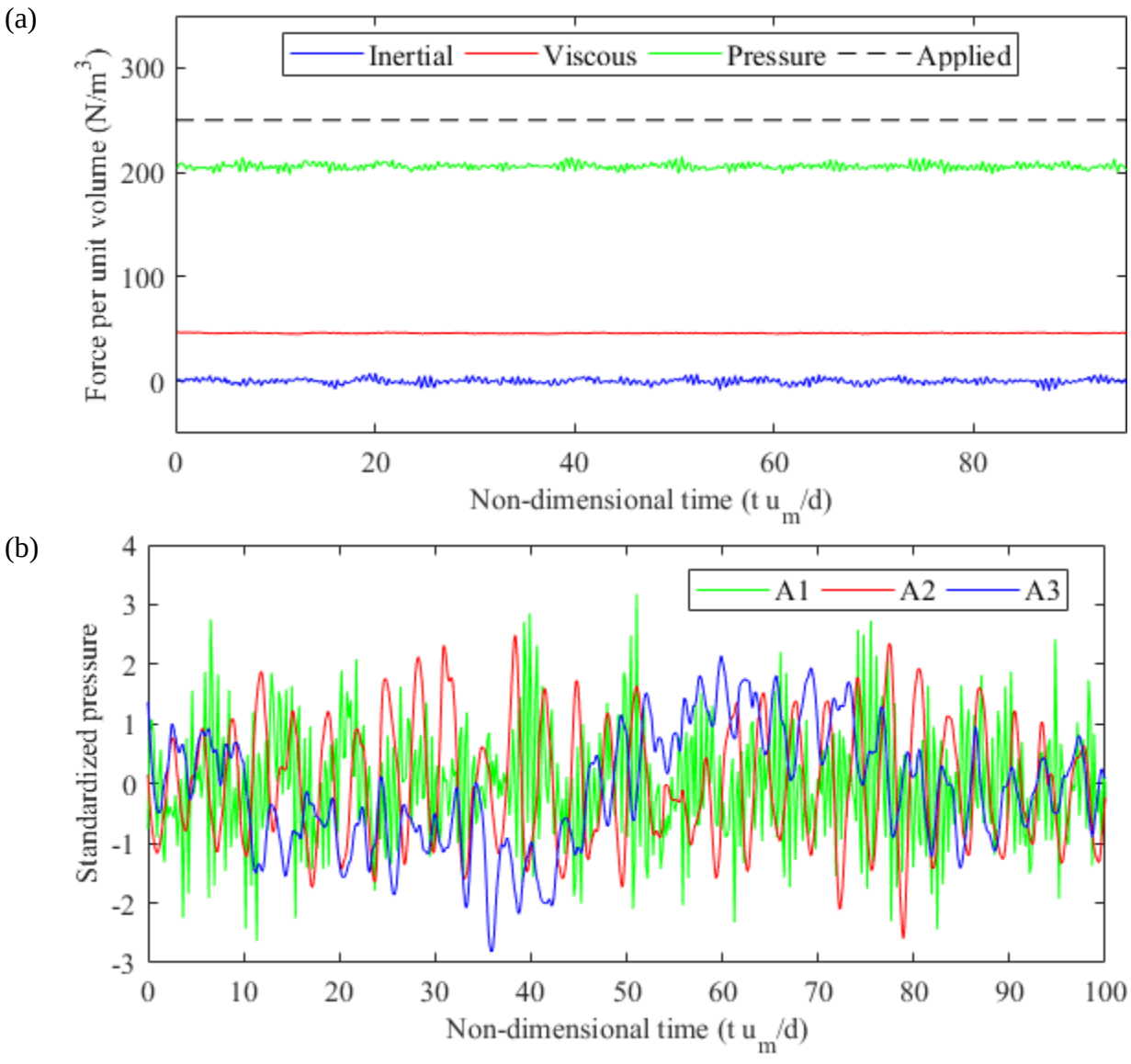

Figure 4.8 (a) Momentum balance of forces in the *x*-direction within a REV for a flow in a porous medium composed of circular cylinders, $\varphi = 0.50$ and $Re_p = 300$ (case A1). (b) Comparison of standardized pressure force for cases A1, A2, and A3.

4.4.4 Correlation Between Heat Transfer and Flow Instabilities

The flow stagnation affects the intensity of vortex shedding, which can be seen in the change of the pressure force oscillation amplitude over time. To observe the correlation between heat transfer and the effects of flow stagnation and vortex shedding, the surface heat transfer rate is represented by the Mean Nusselt Number (Nu_m); the effects of flow stagnation and vortex shedding, which can be seen in the change in pressure force, is represented by the Drag Coefficient (C_d). To separate the vortex shedding and flow stagnation effects that are in the force signal, the FFT of the signals was computed (**Figure 4.9**). The amplitude of both the C_d and Nu_m signals are converted to power (dB), as shown in equation (4.11), for comparison.

$$Power(\mathrm{P}) = 10 * log_{10}(\frac{P}{P_m}) \ \ \mathrm{dB} \tag{4.11}$$

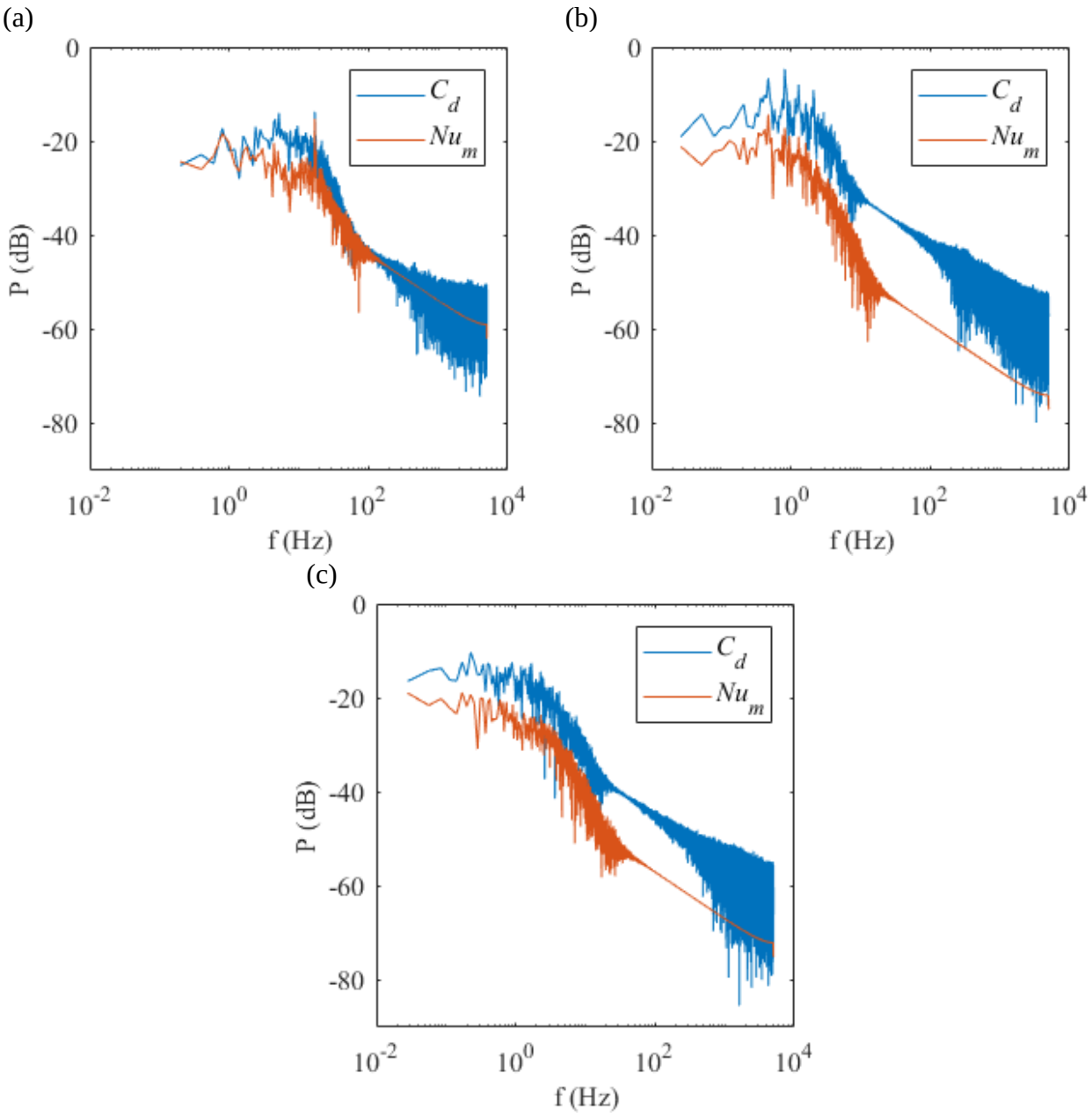

Figure 4.9 Fast Fourier Transform (FFT) of the Drag Coefficient (C_d) and Mean Nusselt Number (Nu_m) for (a) Case A1, $\varphi = 0.50$ with circular obstacles; (b) Case A2, $\varphi = 0.87$ with circular obstacles; (c) Case A3, $\varphi = 0.87$ with square obstacles.

The FFT of the drag coefficient at $\varphi = 0.50$ reveals a lower frequency peak that represents flow stagnation, then a spectrum of frequencies representing the vortex shedding.

Comparing C_d and Nu_m in case A1 (**Figure 4.9** (a)) we can see a correlation between the two signals, which provides evidence that the dynamics of heat transfer is caused by the effects of vortex shedding and flow stagnation. The case A2 (**Figure 4.9** (b)) shows no dominant frequency, but rather a spectrum of frequencies. The lower frequency represents the fact that flow stagnation is still present, but vortex shedding is no longer constrained to a predominant frequency. The change in frequency distribution occurs because the vortices are given more space to develop due to the increase of distance between the obstacle walls. The space allows for the vortex shedding to interact and propagate with the primary flow, resulting with a wider range of frequencies in the change of C_d. Case A3 shows similar traits to A2, but with a smaller amplitude in power. Compared to circular obstacles, the sharp corners of the square obstacle shape restrict the location of the separation points to change over time. This results in a smaller amplitude of intensity when vortices periodically form and dissipate, which shows as smaller power amplitudes (P in **Figure 4.9**) in the FFT of C_d and Nu_m. The combined effect of vortex shedding, and flow stagnation is missing from the steady state RANS result and is captured in the LES simulation, causing ~17% difference between the Nu_m values predicted by these simulations. The signals diverge above the frequency of ~10^2, which indicates there is no direct relation between heat transfer and flow at these higher frequencies (smaller eddies do not impact surface Nu_m).

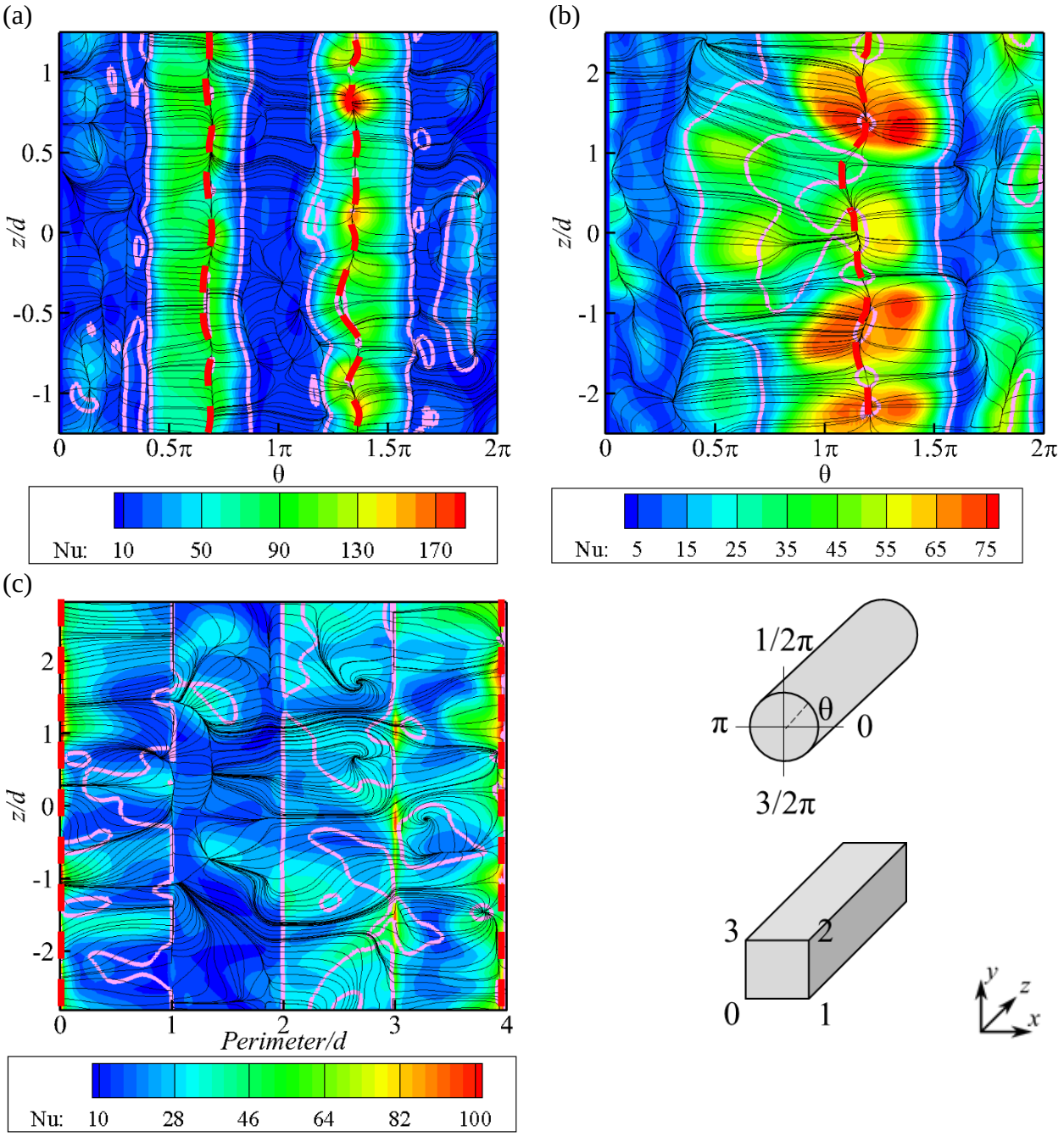

Figure 4.10 Skin-friction lines (black) plotted on the surface of the solid obstacles. Iso-lines (pink) of zero shear stress indicate flow separation and cusp of the skin friction lines (red) indicating the locations of flow stagnation (referred to as stagnation lines). (a) Case A1 (b) Case A2 (c) Case A3.

The surface of the obstacles for cases A1, A2 and A3 are plotted in **Figure 4.10**. There are two band shaped regions with high Nu surrounding the two stagnation lines for case A1 (**Figure 4.10** (a)). While there is only one band of high Nu for case A2 (**Figure 4.10** (b)), the region is wider and oscillates with the change of the position of the stagnation line. For case A3, the high Nu regions are located close to corners 3 and 4 of the obstacle (**Figure 4.10** (c)). This is due to the way the vortices are shed and pushed out from between two obstacles (**Figure 4.7**), forcing the location of the stagnation lines to stay near the corners.

The shed vortices are smaller and more frequent for case A1 compared to the other two cases (**Figure 4.8** and **Figure 4.10** (a)). The vortex structures have a tubular shape elongated in the z- direction. Deformations are observed in the z- direction, which are a product of turbulence. There is a region in between obstacles where vortices are "trapped" forming recirculating vortices and relatively low Nu (<10) is observed on the surfaces in contact with these vortices. Shedding vortices are larger and less frequent for cases A2 and A3 (**Figure 4.8** and **Figure 4.10** (b)(c)). The vortex structures for case A2 are more 3-D and there are no recirculating vortices in these two cases. Because the vortices are in contact with the primary flow region, it enhances mixing and creates regions of relatively high Nu outside the stagnation line region.

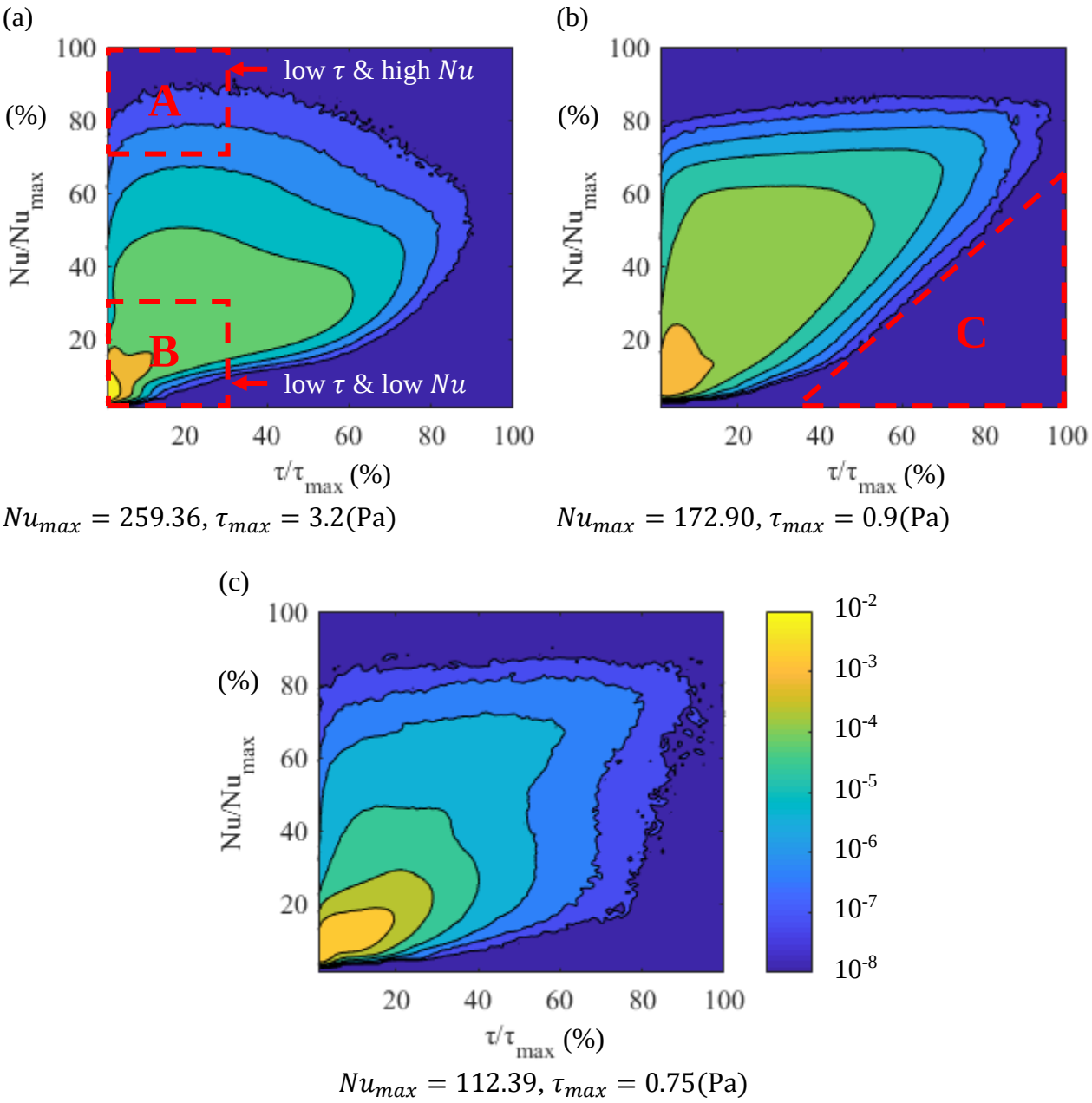

Figure 4.11 Probability Density Function (PDF) for surface Nusselt number (Nu/Nu_{max}) vs shear stress (τ/τ_{max}) for (a) Case A1, $\varphi = 0.50$ with circular obstacles; (b) Case A2, $\varphi = 0.87$ with circular obstacles; (c) Case A3, $\varphi = 0.87$ with square obstacles.

Table 4.4 Percentage of surface heat transfer (Q) over total surface heat transfer (Q_{total}) on each obstacle.

Q/Q_{total}			Surface area of Nu/Nu_{max} and τ/τ_{max} both below 30%
Case	Probability Density > 10^{-3} (yellow areas)	$\tau/\tau_{max} < 30$	
A1 $\varphi = 0.50$	72%	71%	76%
A2 $\varphi = 0.87$	47%	70%	61%
A3 $\varphi = 0.87$ (sq)	87%	93%	94%

The Probability Density Function (PDF) representing the surface Nusselt number vs shear stress (τ) (**Figure 4.11**) shows that more than a half of the obstacle surface area (> 61%) is under low τ and low Nu conditions (region B in **Figure 4.11**), which represents the majority of the obstacle surface (**Table 4.4**). The cases A1 and A3 (**Figure 4.11** (a) and (c)) are characterized by higher probability density areas representing low τ and low Nu conditions. In the case A2 (**Figure 4.11** (b)), the distribution is more spread out. From the FFT of C_d and Nu_m as well as the observation of the surface Nu distribution and shear lines on the obstacle surface, this is because, for case A2, the vortex shedding is not constrained to a predominant frequency compared to the other two cases.

The data points that are located in the low τ and high Nu areas (Region A in **Figure 4.11**) of the PDF are from surface areas that are near the stagnation points in contact with the primary flow (**Figure 4.10**). When recirculating or shedding vortices encounter the downstream obstacle

surface, the lower temperature fluid is entrained from the primary flow by the vortex. There are no data points in region C of **Figure 4.11**, indicating that the condition with low Nu and high τ rarely occurs. In general, a location of low Nu will also have low τ, but not vice versa.

4.5 Conclusions

Micro-vortices play an essential role in porous media flow, and by extension, in convection heat transfer in porous media. The FFT of Nu_m and C_d signals show a match in dominant frequencies, which is supported by flow visualization of cases A1, A2 and A3. This confirms our hypothesis that vortex shedding and flow stagnation are characterized by the time dependent dynamics that predominantly affects heat transfer.

The occurrence of vortex shedding and flow stagnation are sensitive to the porosity and obstacle shapes of the porous medium. For a porous medium composed of circular cylinders, in the case A1 ($\varphi = 0.50$ with circular obstacles), both vortex shedding and flow stagnation occur. When porosity is increased to $\varphi = 0.87$ (case A2), vortex shedding is characterized by a spectrum of frequencies and there is no longer a dominant frequency. It is likely that the change in frequency distribution is because flow in porous media with higher porosity behaves closer to that of open flow over an isolated obstacle. When changing the obstacle shape to square cylinders, case A3 ($\varphi = 0.87$ with square obstacles), the sharp corners of the square obstacle restrict the location of the separation points. This results in a frequency distribution that is similar to case A2, but with a smaller amplitude in power due to the restriction from the obstacle shape.

Further investigations are needed to establish the role of time dependent dynamics of vortex shedding and flow stagnation on heat transfer at higher Reynolds numbers.

CHAPTER 5

Conclusions and Future Work

5.1 Conclusions

From analyzing the turbulence intensity and turbulence length scale, our results support the hypothesis, first expressed in Jin et al. [2], which states that the turbulence length scale is restricted by the surfaces of the surrounding obstacles. The turbulence length scale thus should be comparable to the pore size. We also observed an interesting phenomenon in low porosity cases of $\varphi \leq 0.717$ ($d/s = 0.6{\sim}0.8$), where the bulk flow direction deviates from the driving force direction, and the flow becomes non-symmetric, even though the boundary conditions and geometry are symmetric.

The rate of heat transfer between the obstacle surface and the fluid is influenced by the size of the contact area of the vortices that are attached to the solid obstacles in the porous medium. Although the contact area between the vortices and the obstacle surface, A_{vc}, has a considerable effect on the overall heat transfer from the obstacle to the fluid, it is not as significant compared to the effect of the Pore Scale Reynolds number Re_p. However, in practice, increasing the Reynolds number requires using a larger applied pressure gradient to drive the flow faster. Our results show that by manipulating the vortex contact area with the obstacle by modifying such parameters as the obstacle shape or porosity while keeping the Reynolds number the same, the overall heat transfer rate between the obstacles and fluid can be increased in an "economical" way, without increasing the applied pressure gradient.

Micro-vortices play an essential role in porous media flow, and by extension, in convection heat transfer in porous media. The vortices that are in contact with the solid obstacles can be categorized as recirculating and shedding vortices. The effect of recirculating vortices are less time dependent compared to vortex shedding. Vortex shedding and flow stagnation are characterized by the time dependent dynamics that predominantly affects heat transfer. The occurrence of vortex shedding and flow stagnation are sensitive to the porosity and obstacle shapes of the porous medium. The change of the range in vortex shedding frequency is observed when changing both the porous medium porosity and the shape of the obstacles. It is likely that the change in frequency distribution is because flow in porous media with higher porosity behaves closer to that of open flow over an isolated obstacle.

5.2 Future Work

This thesis presents studies for heat convection in turbulent porous media flow. A basic geometry consisting of cylindrical cylinders arranged in a simple square lattice to represent a homogeneous, anisotropic porous medium. More complex porous medium geometries are yet to be investigated. Surface roughness of the porous medium obstacle, arrangement of the cylindrical obstacles and obstacle shapes that change in the z -direction (such as spheres) are some of the areas we plan to investigate going forward. The range of Re_p in this work is limited by the computational resource and timeframe. Investigations of higher Re_p conditions are of interest to give a more complete picture of the microscale turbulent structures in porous media flow. Time dependent dynamics of vortex shedding and flow stagnation are likely sensitive to Re_p.

From chapter 4, we know that the vortex shedding has a spectrum of different frequencies under different conditions. It would be valuable to investigate what parameters affect these frequencies and whether there are dominant “modes” in these shedding frequencies.

REFERENCES

[1] D.A. Nield, A. Bejan, Convection in porous media, 5th ed., Springer, New York, 2017. https://doi.org/10.1007/978-3-319-49562-0.

[2] Y. Jin, M.-F. Uth, A.V. Kuznetsov, H. Herwig, Numerical investigation of the possibility of macroscopic turbulence in porous media: a direct numerical simulation study, J. Fluid Mech. 766 (2015) 76–103. https://doi.org/10.1017/jfm.2015.9.

[3] M. de Lemos, Turbulence in porous media: modeling and applications, Elsevier, 2012. http://books.google.com/books?hl=en&lr=&id=Rh9XQ_rce9oC&oi=fnd&pg=PP2&dq=Turbulence+in+Porous+Media+MODELING+AND+APPLICATIONS&ots=7vtc9uIn5p&sig=GFUCxfprQhhqSTYKA9p508AoB6o (accessed April 29, 2018).

[4] L. Kum-Bae, J.R. Howell, Theoretical and experimental heat and mass transfer in highly porous media, Int. J. Heat Mass Transf. 34 (1991) 2123–2132. https://doi.org/10.1016/0017-9310(91)90222-Z.

[5] P.J. Prescott, F.P. Incropera, The Effect of Turbulence on Solidification of a Binary Metal Alloy With Electromagnetic Stirring, J. Heat Transfer. 117 (1995) 716. https://doi.org/10.1115/1.2822635.

[6] B.V. Antohe, J.L. Lage, A general two-equation macroscopic turbulence model for incompressible flow in porous media, Int. J. Heat Mass Transf. 40 (1997) 3013–3024. https://doi.org/10.1016/S0017-9310(96)00370-5.

[7] D.A. Nield, The limitations of the Brinkman-Forchheimer equation in modeling flow in a saturated porous medium and at an interface, Int. J. Heat Fluid Flow. 12 (1991) 269–272. https://doi.org/10.1016/0142-727X(91)90062-Z.

[8] D.A. Nield, Alternative Models of Turbulence in a Porous Medium, and Related Matters,

J. Fluids Eng. 123 (2001) 928. https://doi.org/10.1115/1.1413246.

[9] M.-F. Uth, Y. Jin, A. V. Kuznetsov, H. Herwig, A direct numerical simulation study on the possibility of macroscopic turbulence in porous media: Effects of different solid matrix geometries, solid boundaries, and two porosity scales, Phys. Fluids. 28 (2016) 065101. https://doi.org/10.1063/1.4949549.

[10] Y. Jin, A. V. Kuznetsov, Turbulence modeling for flows in wall bounded porous media: An analysis based on direct numerical simulations, Phys. Fluids. 29 (2017) 045102. https://doi.org/10.1063/1.4979062.

[11] A.V. Kuznetsov, Numerical modeling of turbulent flow in a composite porous/fluid duct utilizing a two-layer k–ε model to account for interface roughness, Int. J. Therm. Sci. 43 (2004) 1047–1056. https://doi.org/10.1016/j.ijthermalsci.2004.02.011.

[12] A.V. Kuznetsov, What we can learn from direct numerical simulation of turbulence in porous media : modeling turbulent flow in composite porous/fluid domains, (2017). https://repository.up.ac.za/handle/2263/62364 (accessed April 29, 2018).

[13] H. Nakamura, T. Igarashi, Variation of Nusselt number with flow regimes behind a circular cylinder for Reynolds numbers from 70 to 30000, Int. J. Heat Mass Transf. 47 (2004) 5169–5173. https://doi.org/10.1016/j.ijheatmasstransfer.2004.05.034.

[14] F. Kuwahara, A. Nakayama, Numerical Modeling of Non-Darcy Convective Flow in a Porous Medium, Heat Transf. Proc.11th IHTC. 4 (1998) 411–416. http://www.dbpia.co.kr/Journal/ArticleDetail/NODE00337993 (accessed January 23, 2019).

[15] J.F. McCarthy, Flow through arrays of cylinders: Lattice gas cellular automata simulations, Phys. Fluids. 6 (1994) 435–437. https://doi.org/10.1063/1.868341.

[16] C.-W. Huang, V. Srikanth, K. Andrey V., Effect of Microscale Turbulent Structures Dynamics on Forced Convection in Turbulent Porous Media Flow, in: 5th-6th Therm. Fluids Eng. Conf., 2021.

[17] B.D. Wood, X. He, S. V. Apte, Modeling Turbulent Flows in Porous Media, Annu. Rev. Fluid Mech. (2020). https://doi.org/10.1146/annurev-fluid-010719-060317.

[18] M.J.S. de Lemos, Turbulence in porous media: modeling and applications, Elsevier, Instituto Tecnológico de Aeronáutica—ITA, Brazil, 2012. https://doi.org/10.1016/C2011-0-06981-8.

[19] J.L. Lage, M.J.S. De Lemos, D.A. Nield, Modeling Turbulence in Porous Media, in: Transp. Phenom. Porous Media II, 2007: pp. 198–230. https://doi.org/10.1016/b978-008043965-5/50009-x.

[20] K. Vafai, Handbook of porous media, third edition, 2015. https://doi.org/10.1201/b18614.

[21] K. Vafai, A. Bejan, W.J. Minkowycz, K. Khanafer, A Critical Systhesis of Pertinent Models for Turbulent Transport through Porous Media, in: Handb. Numer. Heat Transf. Second Ed., 2006. https://doi.org/10.1002/9780470172599.ch12.

[22] J.C. Slattery, Flow of viscoelastic fluids through porous media, AIChE J. 13 (1967) 1066–1071. https://doi.org/https://doi.org/10.1002/aic.690130606.

[23] P. Kundu, V. Kumar, I.M. Mishra, Numerical modeling of turbulent flow through isotropic porous media, Int. J. Heat Mass Transf. (2014). https://doi.org/10.1016/j.ijheatmasstransfer.2014.03.020.

[24] A.N. F Kuwahara, Numerical modelling of non-Darcy convective flow in a porous medium, in: Heat Transf. Proc.11th IHTC, 1998. http://www.dl.begellhouse.com/download/article/0a7358c521bfead8/411-416.pdf

(accessed January 22, 2019).

[25] M.H.J. Pedras, M.J.S. De Lemos, Computation of turbulent flow in porous media using a low-reynolds k-ε Model and an infinite array of transversally displaced elliptic rods, Numer. Heat Transf. Part A Appl. (2003). https://doi.org/10.1080/10407780307349.

[26] H. Iacovides, B. Launder, A. West, A comparison and assessment of approaches for modelling flow over in-line tube banks, Int. J. Heat Fluid Flow. 49 (2014) 69–79. https://doi.org/10.1016/j.ijheatfluidflow.2014.05.011.

[27] Y. Jin, M.-F. Uth, A.V. Kuznetsov, H. Herwig, Numerical investigation of the possibility of macroscopic turbulence in porous media: a direct numerical simulation study, J. Fluid Mech. 766 (2015) 76–103. https://doi.org/10.1017/jfm.2015.9.

[28] M.F. Uth, Y. Jin, A. V. Kuznetsov, H. Herwig, A direct numerical simulation study on the possibility of macroscopic turbulence in porous media: Effects of different solid matrix geometries, solid boundaries, and two porosity scales, Phys. Fluids. 28 (2016). https://doi.org/10.1063/1.4949549.

[29] Y. Jin, A. V. Kuznetsov, Turbulence modeling for flows in wall bounded porous media: An analysis based on direct numerical simulations, Phys. Fluids. 29 (2017). https://doi.org/10.1063/1.4979062.

[30] X. He, S. V. Apte, J.R. Finn, B.D. Wood, Characteristics of turbulence in a face-centred cubic porous unit cell, J. Fluid Mech. (2019). https://doi.org/10.1017/jfm.2019.403.

[31] F. Kuwahara, A. Nakayama, Numerical Modelling of Non-Darcy Convective Flow in a Porous Medium, in: Proc. 11th Int. Heat Transf. Conf. IHTC-11, 1998: pp. 411–416.

[32] X. Chu, G. Yang, S. Pandey, B. Weigand, Direct numerical simulation of convective heat transfer in porous media, Int. J. Heat Mass Transf. 133 (2019) 11–20.

[33] K. Suga, R. Chikasue, Y. Kuwata, Modelling turbulent and dispersion heat fluxes in turbulent porous medium flows using the resolved LES data, Int. J. Heat Fluid Flow. (2017). https://doi.org/10.1016/j.ijheatfluidflow.2017.08.005.

[34] F.D. Rocamore Jr., Heat Transport Modeling for Laminar and Turbulent Flows in Porous Media, Instituto Tecnologico de Aeronautica, Brazil, 2001.

[35] M.H.J. Pedras, M.J.S. de Lemos, Thermal dispersion in porous media as a function of the solid-fluid conductivity ratio, Int. J. Heat Mass Transf. (2008). https://doi.org/10.1016/j.ijheatmasstransfer.2008.04.030.

[36] M. Torabi, M. Torabi, M.E. Yazdi, G.P. Peterson, Fluid flow, heat transfer and entropy generation analyses of turbulent forced convection through isotropic porous media using RANS models, Int. J. Heat Mass Transf. (2019). https://doi.org/10.1016/j.ijheatmasstransfer.2018.12.020.

[37] A. Shams, F. Roelofs, E.M.J. Komen, E. Baglietto, Large eddy simulation of a randomly stacked nuclear pebble bed, Comput. Fluids. (2014). https://doi.org/10.1016/j.compfluid.2014.03.025.

[38] X. Li, X. Wu, Thermal mixing of the cross flow over tube bundles, Int. J. Heat Mass Transf. (2013). https://doi.org/10.1016/j.ijheatmasstransfer.2013.08.031.

[39] ANSYS Inc., Fluent User's Guide, Release 1, 2018.

[40] T.H. Shih, W.W. Liou, A. Shabbir, Z. Yang, J. Zhu, A new k-ε{lunate} eddy viscosity model for high reynolds number turbulent flows, Comput. Fluids. 24 (1995) 227–238. https://doi.org/10.1016/0045-7930(94)00032-T.

[41] R.L. Panton, Incompressible Flow, John Wiley & Sons, Inc., Hoboken, NJ, USA, 2013. https://doi.org/10.1002/9781118713075.

[42] H. Iacovides, B. Launder, A. West, A comparison and assessment of approaches for modelling flow over in-line tube banks, Int. J. Heat Fluid Flow. 49 (2014) 69–79. https://doi.org/10.1016/j.ijheatfluidflow.2014.05.011.

[43] V. Srikanth, C.-W. Huang, T.S. Su, A. V. Kuznetsov, Symmetry Breaking in Porous Media as a Consequence of the von Karman Instability, ArXiv. (2018).

[44] V. Srikanth, C.W. Huang, T.S. Su, A. V. Kuznetsov, Symmetry Breaking in Porous Media as a Consequence of the von Karman Instability, (2018). https://arxiv.org/abs/1810.10141 (accessed January 22, 2019).

[45] M. Kaviany, Principles of Heat Transfer in Porous Media, Springer US, New York, NY, 1991. https://doi.org/10.1007/978-1-4684-0412-8.

[46] W.W. Kim, S. Menon, Application of the localized dynamic subgrid-scale model to turbulent wall-bounded flows, in: 35th Aerosp. Sci. Meet. Exhib., 1997.

[47] I.B. Celik, Z.N. Cehreli, I. Yavuz, Index of Resolution Quality for Large Eddy Simulations, J. Fluids Eng. (2005). https://doi.org/10.1115/1.1990201.

[48] S.B. Pope, Ten questions concerning the large-eddy simulation of turbulent flows, New J. Phys. 6 (2004) 35. https://doi.org/10.1088/1367-2630/6/1/035.

[49] V. Srikanth, C.W. Huang, T.S. Su, A. V. Kuznetsov, Symmetry breaking in porous media as a consequence of the von karman instability, ArXiv. (2018).

[50] M.J.S. de Lemos, Turbulence in Porous Media, 2006. https://doi.org/10.1016/B978-0-08-044491-8.X5000-0.

APPENDICES

Appendix A

RANS Model Validation

The commercial code ANSYS Fluent 16.0 is used to simulate the cases for this supplementary study, similar to the main paper. However, a RANS turbulence model is used to simulate the flow. The Realizable k-ε model is chosen in this work. All of the RANS turbulence models available in ANSYS Fluent 16.0 that may be suitable for this flow are validated against case B2 in the main paper (φ=0.5, Re_p = 1,000, circular cylinder obstacles). The validation results are presented in figure S1. The Realizable k-ε model agrees with the LES results with an error of ~20% in the velocity field. It is deemed acceptable for this supplementary study based on qualitative agreement with LES and is used for all of the simulations presented below.

The steady-state RANS governing equations are discretized using the Finite Volume Method. Second-order upwind schemes are used for all of the spatial derivatives. The governing equations are solved iteratively till a convergence tolerance of 10^{-4} is reached. Sensitivity to the convergence tolerance has been tested using the values 10^{-3}, 10^{-4}, 10^{-5}, 10^{-6}, and 10^{-7}. Tolerance values below 10^{-4} yielded identical surface skin friction plots.

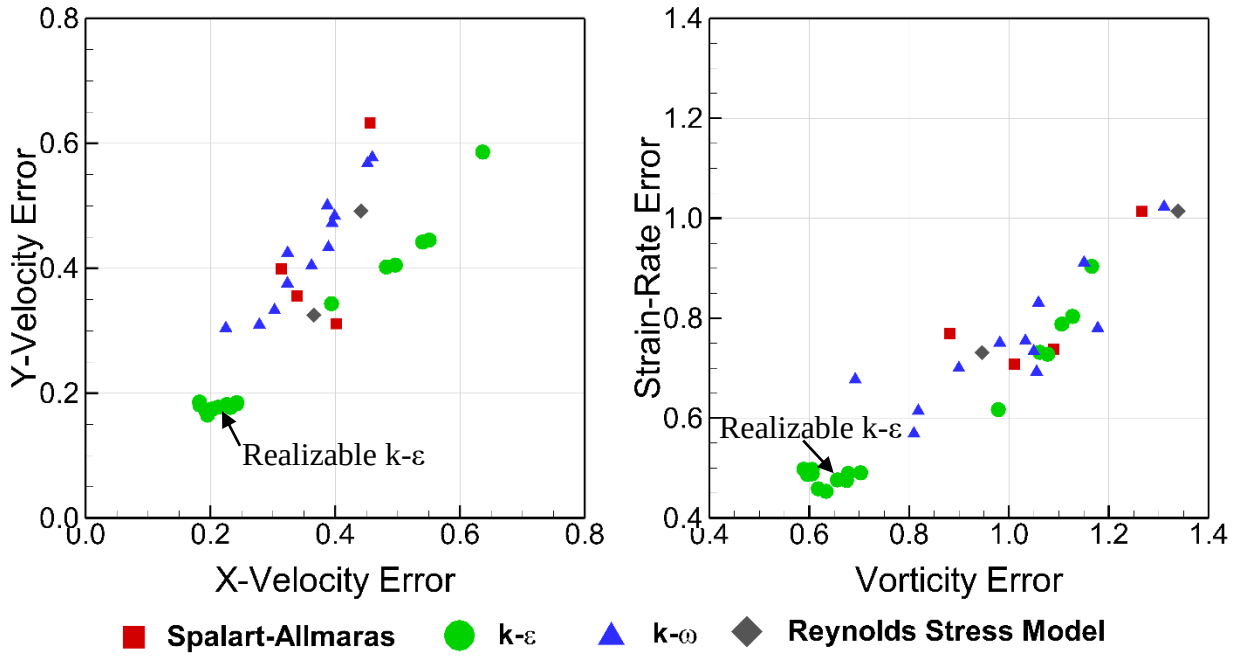

Figure A.1 The RANS model error for the validation case when compared to LES for the quantities – *x*- and *y*- velocity, strain rate and vorticity. Each point on the chart corresponds to a unique turbulence model and the symbols correspond to a model class. Square – Spalart-Allmaras models, circle – k-ε models, triangle – k-ω models, diamond – Reynolds stress models.

The numerical method outlined above is used to simulate turbulent flow with different geometric parameters at Re_p = 10,000.

Appendix B

Validation of the size of the REV-T

In this section, the convergence of the macroscale flow solution at the chosen REV size is demonstrated. The turbulent structures will be restricted the least at the porosity of 0.8 by the solid boundaries of the obstacles. If the REV size is adequate for φ = 0.8, it is reasonable to assume that it will be adequate for cases with lower porosity. At φ = 0.8, the solid obstacle shape has the least influence on the macroscale properties among all of the cases. A Reynolds number of 1,000 is chosen since a majority of cases assume this value or lesser. Unlike Re_p = 225, the flow at Re_p = 1,000 is not close to the turbulence transition point and is, therefore, representative of the limiting cases of turbulence transport in this paper with regard to REV size.

With these parameters fixed, the REV size is increased from 1*s* to 5*s* in increments of 1*s*. A grid resolution of 0.02*s* is used to perform LES for each of the REV sizes. Two macroscale quantities are analyzed in this study: the mean applied momentum source $\langle g_i \rangle$, and the macroscale TKE $\langle k \rangle^i$ (**Figure A.2**). The applied momentum source term is directly linked to the drag force on the surface of the solid obstacles inside the porous medium. The macroscale TKE indicates whether an adequate sample of the turbulence fluctuations is captured by the REV. Both $\langle g_i \rangle$ and $\langle k \rangle^i$ converge at an REV size of 4*s* with changes of only 0.4% and 0.25% respectively when the REV size is increased to 5*s*. When the size of the REV is increased from 1*s*, there is a staggered trend observed depending on whether an odd or even number of obstacles are present in the REV. The cause of the staggering is a decoupling between the odd and even number REVs. The decoupling is brought about by the influence of the periodic boundary condition that is imposed, and also the number of modes of the microscale flow instability that can be present in the domain. The distinction between the odd and even number REVs

diminishes at the REV size of 4*s*. This offers further confirmation that the REV size of 4*s* is adequate for the simulations presented in this paper. We decreased the REV size in the *z*-direction for cylindrical solid obstacle geometries from 4*s* to 2*s*. The turbulence two-point correlation function was found to de-correlate in the *z*- direction in a span of 1*s*. The turbulent structure visualizations also showed smaller structure size in the *z*- direction.

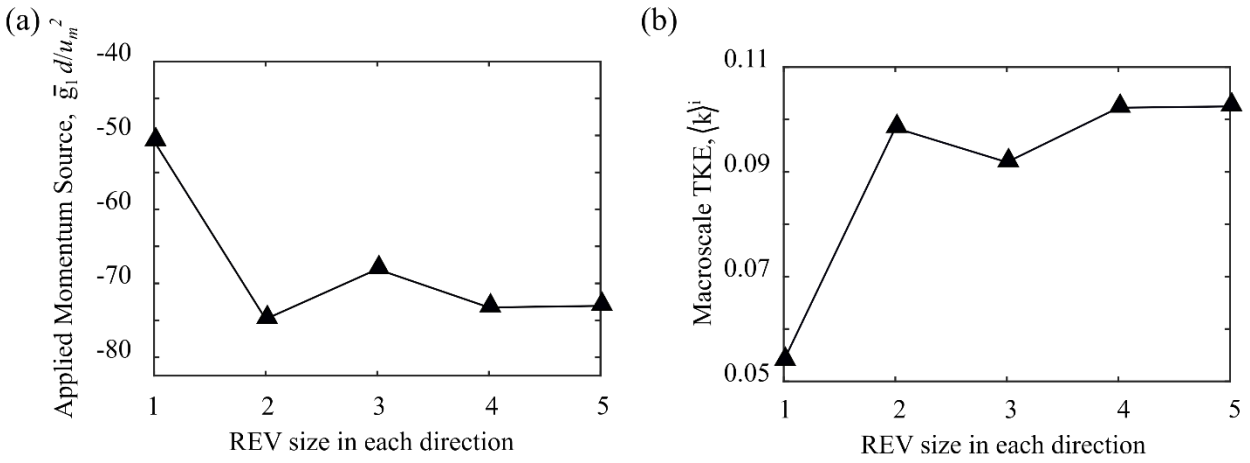

Figure A.2 The convergence of the (a) applied momentum source and (b) the macroscale TKE with increase in the REV size.